Automating the tuning and matching process of a sixteen-channel transmit-only TEM array with a thirty-two-channel receive-only loop array for body imaging applications at 7T

A DISSERTATION
SUBMITTED TO THE FACULTY OF THE GRADUATE SCHOOL
OF THE UNIVERSITY OF MINNESOTA
BY

Carl J. Snyder

IN PARTIAL FULFILLMENT OF THE REQUIREMENTS
FOR THE DEGREE OF
DOCTOR OF PHILOSOPHY

Dr. J. Thomas Vaughan

September 2013

To my beautiful wife, Angela

and my new son, Luke.

Table of Contents

List of Tables

List of Figures

Preface

This thesis is structured around three journal articles. The first three chapters provide the background for the three articles. The three articles are all concerned with advancements in RF array design that have made 7T body imaging possible. The first two articles, are previously published and provide background for the final, which has yet to be submitted. The first article, presented in chapter four, was originally published in 2009 outlines and describes a novel TEM surface array that allowed for the first successful cardiac imaging at 7T. The second article, presented in chapter five, presents a comprehensive comparison between two similar TEM arrays; in many respects this article has set the standard for array evaluations and comparisons. The third and final article, presented in chapter six is concerned with ongoing research. It outlines a sixteen-channel TEM transmit-only array used in conjunction with a thirty-two-channel loop receive-only array. Additionally, to address the difficulty of tuning and matching a sixteen-channel array, a novel automated tuning and matching process using an electromechanical solution is presented.

1. Fundamentals of Magnetic Resonance

1.1 Nuclear Magnetic Resonance

Magnetic resonance is a physical phenomenon that occurs when a magnetic dipole interacts with a magnetic field. When placed in a magnetic field, a magnetic dipole can only absorb or emit energy in a form of electromagnetic radiation at specific frequencies. Most subatomic particles, namely electrons, protons and neutrons have an intrinsic magnetic dipole due to their quantum mechanical spin. Quantum spin is an intrinsic form of angular momentum carried by elementary particles, composite particles (hadrons), and atomic nuclei. In most atomic nuclei, protons and neutrons combine such that their intrinsic spins cancel out, leaving the nucleus magnetically inert. In some nuclei however, the spins do not cancel each other, and a magnetic moment occurs. The magnetic moment $\vec{\mu}$, is related to the spin, $\vec{J}$, by a magnetogyric ratio, γ.

$$\vec{\mu} = \gamma \vec{J} \tag{1}$$

Nuclei with magnetic moment will naturally try to align itself with an external magnetic field. The dipole experiences a torque,T, perpendicular to it's magnetic moment and the external magnetic field, B_0.

$$T = \mu \cdot B_0 \tag{2}$$

Due to the constant angular momentum of the nucleus cannot align with the magnetic field, B_0; it will instead gyroscopically precess about the external field axis at a consant rotational velocity called the Larmor frequency:

$$\omega_o = \gamma \, B_o \tag{3}$$

As stated earlier dipoles will try to align with the external magnetic field. Some of the dipoles will align with the magnetic field and be at a lower energy level then the dipoles that align against the external field. The difference between these two energy levels, ΔE, is

$$\Delta E = \omega_o \hbar \tag{4}$$

where $\hbar$ is Planck's constant (6.6 x 10^{-34} J-s) divided by 2π.

Since the dipoles asymmetrically align with the lower energy level, a population difference occurs. In accordance to Boltzmann's relationship, the population difference is related to the difference in energy levels

$$\frac{N_{\downarrow}}{N_{\uparrow}} = e^{-\frac{\Delta E}{KT_s}} \tag{5}$$

where $N_{\uparrow}$ and $N_{\downarrow}$ are the number of dipoles aligned parallel and antiparallel to the field, respectively, K is Boltzmann's constant (1.38 x 10^{-23} J/K) and T_s is the absolute temperature of the sample. While this ratio is very small, it provides the basis for a bulk magnetization vector. The bulk magnetization vector is the sum of all magnetic moments

$$\overrightarrow{M} = \sum_{n=1}^{N_{\uparrow}} \mu_n - \sum_{n=1}^{N_{\downarrow}} \mu_n \tag{6}$$

and is the signal for MR imaging. This magnetization can be described as a vector that is manipulated according to classical equations of motion, which are known as the Bloch equation.

Bloch Equations

The Bloch equation describes how the bulk magnetization vector evolves over time in any magnetic field. It is the cross product of the bulk magnetization vector $\vec{M}$ and the external magnetic field, $\vec{B}$

$$\frac{d\vec{M}}{dt} = -\gamma\ \vec{B} \times \vec{M} \tag{7}$$

Since it is treated as a vector, breaking it into the magnetic components leads to

$$\frac{dM_x}{dt} = \gamma(B_z M_y - B_y M_z) \tag{8}$$

$$\frac{dM_y}{dt} = \gamma(B_x M_z - B_z M_x) \tag{9}$$

$$\frac{dM_z}{dt} = \gamma(B_y M_x - B_x M_y) \tag{10}$$

and at equilibrium, assuming the external field is equal to $\vec{B} = B_o\vec{k}$, (where k is the unit vector in Cartesian coordinate system), the components simplify to

$$\frac{dM_x}{dt} = \gamma B_o M_y \tag{11}$$

$$\frac{dM_y}{dt} = -\gamma B_o M_x \tag{12}$$

$$\frac{dM_z}{dt} = 0 \tag{13}$$

A temporally-short RF pulse is used to tip the dipoles, and bulk magnetization vector, from equilibrium, into the transverse plane. This RF pulse creates an oscillating magnetic field perpendicular to the main magnetic field and affects the bulk magnetization vector in the following manner

$$\frac{dM_x}{dt} = \gamma(B_o M_y - M_z B_{rf} \sin(\omega_{rf} t)) \quad (14)$$

$$\frac{dM_y}{dt} = \gamma(M_z B_{rf} \cos(\omega_{rf} t) - B_o M_x) \quad (15)$$

$$\frac{dM_z}{dt} = \gamma(M_x B_{rf} \sin(\omega_{rf} t) - M_y B_{rf} \cos(\omega_{rf} t)) \quad (16)$$

In order to make the calculations simpler, the frame of reference is changed from the laboratory frame to a reference frame rotating at the RF pulse's frequency. The pulse now loses its time dependence and equations 2.2.4a-c simplify to

$$\frac{dM_{x'}}{dt} = (\omega_o - \omega_{rf}) M_y \quad (17)$$

$$\frac{dM_{y'}}{dt} = (\omega_o - \omega_{rf}) M_x + \gamma B_{rf} M_z \quad (18)$$

$$\frac{dM_{z'}}{dt} = -\gamma B_{rf} M_y \quad (19)$$

where $M_{(x,y,z)'}$ represents the bulk magnetization vector in the rotating frame. Now any change of magnetization is dependant upon the RF pulse. Equations 17-19 simplify even more when the frequency of the RF pulse is centered the Larmor frequency, such that, $\omega_o - \omega_{rf} = 0$. Since this rotating frame of reference is standard in MR imaging, it will be used, and the prime superscripts are implied.

The previously described Bloch Equation 17-19 incompletely describes how a magnetic field affects the bulk magnetization vector. Since the spin system is frictionless, theoretically once the spins are disturbed from equilibrium, they should not return. However due to nuclear dipole interactions, the spins will relax back to their equilibrium values. Noticing this phenomenon Bloch added, ad hoc, two relaxation

terms. The first relaxation term describes the system returning to equilibrium while the second term describes the loss of phase coherence in the transverse plane.

Longitudinal relaxation, also called spin-lattice relaxation, in classical terms, can be described as the bulk magnetization vector returning to equilibrium. In quantum mechanics it's viewed as the spin populations returning to their equilibrium energy values. The longitudinal relaxation is

$$\frac{dM_z}{dt} = \frac{M_z - M_o}{T_1} \tag{20}$$

where T_1 is the spin-lattice relaxation time. This is the time necessary for the longitudinal magnetization vector to recover within 63% (or $1\text{-}e^{-1}$) of the bulk magnetization's equilibrium value.

Transverse relaxation, also called spin-spin relaxation, is the dephasing of the MR signal in the transverse plane. Dephasing of transverse magnetization is

$$\frac{dM_x}{dt} = -\frac{M_x}{T_2} \tag{21}$$

$$\frac{dM_y}{dt} = -\frac{M_y}{T_2} \tag{22}$$

where T_2 is the transverse relaxation time. This is the time at which the transverse magnetization has lost 37% (or e^{-1}) of its original signal, due to dephasing.

Inserting equations 21 and 22 into 20, leads to the complete Bloch equations in the rotating frame of reference.

$$\frac{dM_x}{dt} = (\omega_o - \omega_{rf})M_y - \frac{M_x}{T_2} \quad (23)$$

$$\frac{dM_y}{dt} = (\omega_o - \omega_{rf})M_x + \gamma B_{rf} M_z - \frac{M_y}{T_2} \quad (24)$$

$$\frac{dM_z}{dt} = -\gamma B_{rf} M_y + \frac{M_z - M_o}{T_1} \quad (25)$$

Immediately after a RF pulse is applied, assuming no relaxation during the pulse, the bulk magnetization vector is tipped into the transverse plane. How far it is tipped into the transverse plane, also known as the flip angle, is dependent upon the magnitude of the RF pulse and for how long the RF pulse is applied. For example, a 90° RF pulse will tip or flip the bulk magnetization vector 90° and likewise a 180° RF pulse will flip the bulk magnetization vector 180°. If the RF pulse is applied along the x-axis the resulting components of magnetization are (solutions to Block equations in presence of rf pulse) (26)

$$M_x(0_+) = M_x(0_-)$$

$$M_y(0_+) = M_y(0_-)\cos(\gamma B_{rf} t) + M_z(0_-)\sin(\gamma B_{rf} t) \quad (27)$$

$$M_z(0_+) = -M_y(0_-)\sin(\gamma B_{rf} t) + M_z(0_-)\cos(\gamma B_{rf} t) \quad (28)$$

where $M_n(0_-)$ and $M_n(0_+)$ are the magnitudes of the components of magnetization directly before and after the RF pulse, respectively.

Due to magnetic field inhomogeneities, spins precess at different frequencies, ω. If the spins are as allowed to precess for a time τ, equations 26-28 evolve as (solution to Block equations in absence of rf pulse)

$$M_x(\tau) = \left[M_x(0_+)cos(\omega_0 - \omega)\tau + M_y(0_+)sin(\omega_0 - \omega)\tau\right]e^{\frac{-\tau}{T_2}} \quad (29)$$

$$M_y(\tau) = \left[-M_y(0_+)sin(\omega_0 - \omega)\tau + M_x(0_+)cos(\omega_0 - \omega)\tau\right]e^{\frac{-\tau}{T_2}} \quad (30)$$

$$M_z(\tau) = M_z(0_+)e^{\frac{-\tau}{T_1}} + M_0\left(1 - e^{\frac{-\tau}{T_1}}\right) \quad (31)$$

Understanding the Bloch equations makes solving a series of RF pulses trivial. For example, if a 90° RF pulse is applied along the x-axis, assuming that the bulk magnetization vector is at equilibrium, the components of magnetization are the following:

$$M_x(0_+) = 0 \quad (32)$$

$$M_y(0_+) = M_z(0_-) = M_o \quad (33)$$

$$M_z(0_+) = 0 \quad (34)$$

The components of magnetization of equations 32-34 will precess over time, τ_1, to equal

$$M_x(\tau_1) = M_o \sin(\Delta\omega\tau)e^{\frac{-\tau_1}{T_2}} \quad (35)$$

$$M_y(\tau_1) = -M_o \cos(\Delta\omega\tau)e^{\frac{-\tau_1}{T_2}} \quad (36)$$

$$M_z(\tau_1) = M_o(1 - e^{\frac{-\tau_1}{T_1}}) \quad (37)$$

where $\Delta\omega$ has replaced (ω_o-ω). If another RF pulse is applied, this time a 180° pulse along the y-axis, the components of magnetization at time τ_{1+} become

$$M_x(\tau_{1+}) = -M_o \sin(\Delta\omega\tau)e^{\frac{-\tau_1}{T_2}} \quad (38)$$

$$M_y(\tau_{1+}) = -M_o \cos(\Delta\omega\tau)e^{\frac{-\tau_1}{T_2}} \quad (39)$$

$$M_z(\tau_{1+}) = -M_o(1 - e^{\frac{-\tau_1}{T_1}}) \quad (40)$$

Notice that the only affect of the second RF pulse was to change the signs of the magnetization in the x and z directions. The 180° pulse effectively rotates any magnetization vector 180° around the y-axis. If the components of magnetization are allowed to precess for time τ_2

$$M_x(\tau_2) = M_o(\sin\Delta\omega\tau_1\cos\Delta\omega\tau_2 - \cos\Delta\omega\tau_1\sin\Delta\omega\tau_2)e^{\frac{-(\tau_1+\tau_2)}{T_2}} \quad (41)$$

$$M_y(\tau_2) = M_o(\cos\Delta\omega\tau_1\cos\Delta\omega\tau_2 + \sin\Delta\omega\tau_1\sin\Delta\omega\tau_2)e^{\frac{-(\tau_1+\tau_2)}{T_2}} \quad (42)$$

$$M_z(\tau_2) = -M_o(1-e^{\frac{-(\tau_1+\tau_2)}{T_1}}) \quad (43)$$

Equations 41-43 can be simplified to

$$M_x(\tau_2) = M_o\sin\left[\Delta\omega(\tau_1-\tau_2)\right]e^{\frac{-(\tau_1+\tau_2)}{T_2}} \quad (44)$$

$$M_y(\tau_2) = M_o\cos\left[\Delta\omega(\tau_1-\tau_2)\right]e^{\frac{-(\tau_1+\tau_2)}{T_2}} \quad (45)$$

$$M_z(\tau_2) = -M_o(1-e^{\frac{-(\tau_1+\tau_2)}{T_1}}) \quad (46)$$

Now if we allow $\tau_1 = \tau_2$ and $\tau = \tau_1+\tau_2$then equations 45-46 simplify to

$$M_x(\tau) = 0 \quad (47)$$

$$M_y(\tau) = M_o e^{\frac{-\tau}{T_2}} \quad (48)$$

$$M_z(\tau) = -M_o(1-e^{\frac{-\tau}{T_1}}) \quad (49)$$

From equations 47-49, it is seen that at time τ, the spins refocus and a spin echo occurs. The magnitude of the spin echo is equal to the bulk magnetization vector minus any relaxation effects. The pulse sequence just described, $90°_x$ - τ_1 – $180°_y$ - τ_2, provides the basis for all spin echo imaging sequences

1.2 Signal Localization

Magnetic gradients coils create varying magnetic fields of controlled spatial non-uniformity. It is known that the precessional frequency depends on the magnetic field strength and when a magnetic field gradient is applied to a homogeneous object, spins on one side of the object will precess at a different frequency then the spins on the other side of the object. A distribution of frequencies will be obtained along the sample. In MR imaging three orthogonal coils create the magnetic field gradients. While any combination of the three gradients can be applied at any given time to create spatially dependant precessional frequencies, for simplicity, we will assume that the gradient coil aligned along the z axis creates the slice selection gradient, the coil creating a gradient in the x direction is used for frequency encoding and the gradient in the y direction is used to encode the phase information of the signal.

Slice Selection Gradient, G_{SS}

In imaging the rf pulse is bandwidth limited and only the spins precessing within this bandwidth will be excited. Since the RF pulse is usually centered around the Larmor frequency, if it was applied in the absences of a gradient, all the spins within the sample would be excited and signal would be emitted over the entire sample. However, if a gradient is applied during the RF pulse, such that only a small volume of the sample was precessing within the RF's bandwidth, then only that volume would be excited and emit a signal. In the presence of this gradient, the rest of the spins in the object outside of the RF's bandwidth remain unaffected. This is the slice selection gradient, G_{ss}; in

combinations with the rf pulse, it determines the slice location and the thickness of the slice.

The slice location is dependent upon the frequency of the RF pulse and the strength of the gradient.

$$z = \frac{f_{rf}}{\gamma \, G_{ss}} \tag{50}$$

The thickness of the slice is determined by the bandwidth of the pulse and the strength of the gradient.

$$\Delta z = \frac{bw_{rf}}{\gamma \, G_{ss}} \tag{51}$$

From figure 1 it is easy to see how the RF's frequency, bandwidth, and gradient strength affects the slice location and thickness.

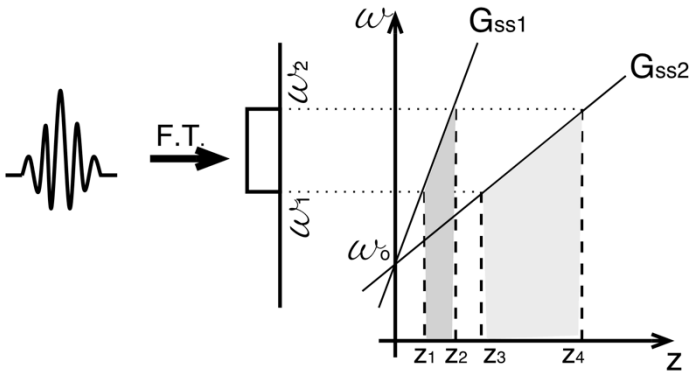

Figure 1: Slice Section Gradient. G_{SS1} is a stronger gradient then G_{SS2}, therefore it provides a thinner slice thickness and shifts the slice location.

Frequency-Encoding Gradient

It was already stated that the spin's precessional frequency in the presence of gradient field depends on spatial location, therefore the different precessional frequencies can be used for spatial localizations. The precessional frequency of a spin in a gradient field is

$$\omega(x) = \omega_o + \gamma G_{fe} x \tag{52}$$

The amount of magnetization at each frequency is the integral of the signal perpendicular to the applied frequency-encoding gradient (fig 2).

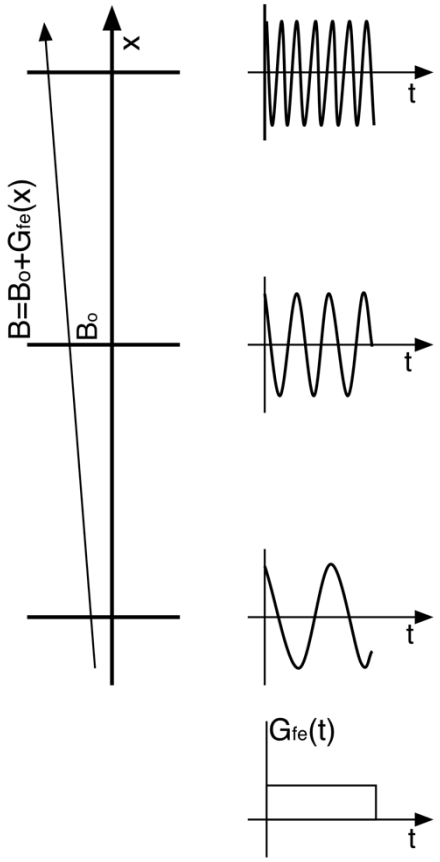

Figure 2: Frequency encoding gradient. The precessional frequency depends on the spatial location of the spin.

Phase-Encoding Gradient

When a gradient is applied, due to different precessional frequencies, there is a loss of phase coherence. If a gradient is applied for a short period of time and then turned off, the dipoles return to precessing at the Larmor frequency, but the phase accumulated while the gradient was applied remains. The accumulation of phase can be used for spatial localization; in MR imaging this is known as phase encoding. The amount of phase, φ_p, a spin accumulated depends on the strength of the gradient and how long the gradient was applied, as seen in equation 53 and figure 3.

$$\varphi_p = \gamma G_{pe} T_{pe} \tag{53}$$

Phase encoding is implemented by applying a gradient orthogonal to both the slice-selection and frequency-encoding gradients. This gradient is applied for a brief time after the excitatory RF pulse but before the signal collection.

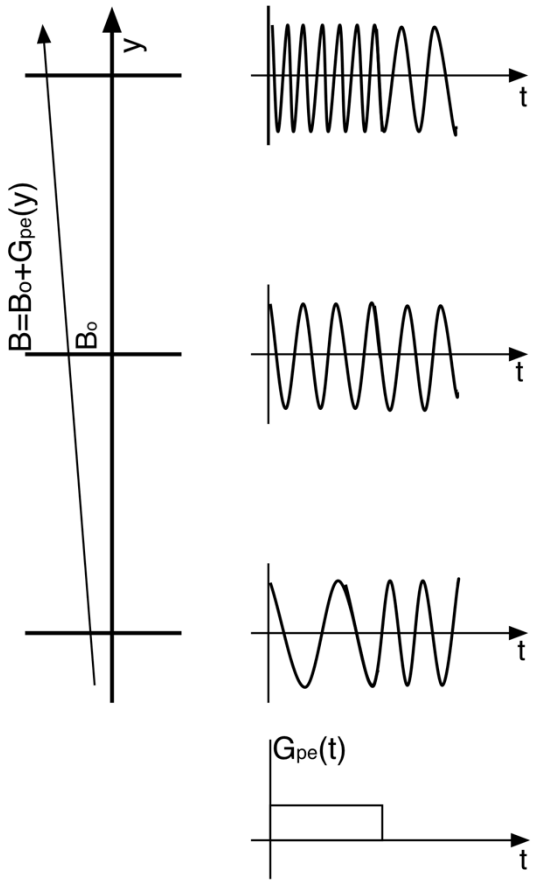

Figure 3: Phase-encoding gradient. After a gradient is turned off, the spins precess at the Larmor frequency, but the phase accumulated while the gradient was applied remains.

It is necessary to show mathematically how the signal evolves over time due to the magnetic gradients. Assuming no relaxation, before any gradients are applied the MR signal is time independent

$$S(t) = \rho \tag{54}$$

where ρ is the magnetization vector in the transverse plane. This is the sum of the entire signal in the imaging plane. After the phase-encoding gradient is applied and removed the signal is still time independent, however, the spins have accumulated differing amounts of phase depending on their spatial location. The signal given off by an

individual spin at a given point y_o, along the phase encoding direction has the following phase on the n^{th} measurement:

$$S_n(t) = \rho(y_o)e^{i\gamma\, nT_{pe}G_{pe}y_o} \tag{55}$$

Collecting the signal while the frequency-encoding gradient is applied creates a time dependence on the n^{th} measurement:

$$\begin{aligned} S_n(t) &= \rho(x_o, y_o)e^{i\gamma\, nT_{pe}G_{pe}y_o}e^{i\gamma\, G_{fe}x_o t} \\ &= \rho(x_o, y_o)e^{i\gamma\,(nT_{pe}G_{pe}y_o + G_{fe}x_o t)} \end{aligned} \tag{56}$$

Equation 56 describes the signal at one point, but the collected signal is the sum of all the individual magnetization vectors at each location in space. This is described by integrating over both x and y

$$S_n(t) = \int_{-\infty}^{\infty}\int_{-\infty}^{\infty}\rho(x,y)e^{i\gamma\,(nT_{pe}G_{pe}y_o + G_{fe}x_o t)}dxdy \tag{57}$$

In order to get an image, it is necessary to find ρ(x, y) from $S_n(t)$. This is performed with an inverse Fourier Transform on $S_n(t)$. To simplify the equation, frequency space of the image is described as K-space. K-space is the inverse Fourier Transform of the image. The spatial frequencies, or conjugate variables, of x and y are k_x and k_y respectively. They are defined as

$$k_x = \frac{\gamma\, G_{fe}t}{2\pi} \tag{58}$$

and

$$k_y = \frac{\gamma\, nG_{pe}T}{2\pi} \tag{59}$$

Substituting equations 2.3.9 and 2.3.10 into equation 2.3.8 leads to

$$S(k_x, k_y) = \int_{-\infty}^{\infty}\int_{-\infty}^{\infty}\rho(x,y)e^{i2\pi\,(k_x x + k_y y)}dxdy \tag{60}$$

Performing an inverse Fourier transform on this, will obtain the image spatial distribution

$$\rho(x,y) = \int_{-\infty}^{\infty}\int_{-\infty}^{\infty} S(k_x,k_y)e^{-2\pi\,(k_x x + k_y y)}dk_x dk_y \tag{61}$$

This inverse Fourier transform provides the image for MR acquisitions. Equation 61 describes how the signal is converted to an image, the physics how the signal is collected, will be discussed next.

2. Loop Resonators and Arrays

Loop coils are simple resonant structures, usually only composed of inductive wire and capacitors. They are easy to design and frequently used in surface arrays because of their well-defined sensitivity profile and minimal interactions with transmit arrays. Figure 4 shows a loop coil and it's lumped element equivalent. From its lumped element equivalent, it is shown that a loop coil is a series resonant RLC circuit.

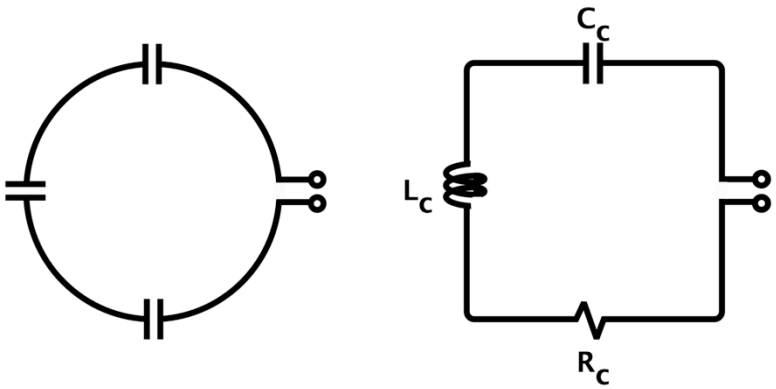

Figure 4: The standard loop coil and it's lumped-element equivalent. The inductance, L_C and resistance (or resistivity), R_C, are based on size and materials of the coil.

2.1 Resonance Condition

By definition, resonance occurs when the average stored magnetic and the electric energies in a circuit are equal. From this, it is known that the inductance and capacitance in the circuit determine resonance and the relation between the angular resonance frequency, ω_O, and the circuit's inductance and capacitance is given by the Thompson formula:

$$\omega_O = \frac{1}{\sqrt{LC}} \tag{63}$$

In terms of MR loop coils and resonators, the inductance is set by the size of the coil and material used, therefore the capacitance is varied to achieve resonance at the appropriate Larmor frequency.

2.2 Input Impedance

The complex impedance of the series RLC lumped element circuit in figure 1 is

$$Z_M = R + j\omega_O L - j\frac{1}{\omega_O C} \tag{64}$$

However, because of the resonance condition, equation 2 reduces to

$$Z_M = R \tag{65}$$

where R is any combination of conductive losses, R_C (which are predominantly the inductive losses in MR coils), radiative losses, R_R, (which are only predominant at high field strengths where the electrical length of a coil exceeds the wavelength of the Larmor frequency) and load losses, R_L, (which, obviously only occur when the coil is coupled to a load).

2.3 Quality Factor

The quality factor (or Q) is a method for characterizing the rate of energy loss from an resonant system. It is defined as the angular resonant frequency times the energy stored in a resonant system divided by the circuits losses over time.

Since the loop coil is a series RLC circuit, the unloaded Q factor is

$$Q = \frac{\omega_O L}{R_C} = \frac{1}{\omega_O R_C C} \tag{66}$$

Here, the conductor losses are identified as majority of the losses, which is true at lower field strengths. At higher field strengths the radiative losses start to dominate. The loaded Q factor, Q_L, of the loop coil is

$$Q_L = \frac{\omega_O L}{R_C + R_L} = \frac{1}{\omega_O (R_C + R_L) C} \tag{68}$$

where the load losses are added to the conductive losses.

2.4 Efficiency, Sensitivity and Signal to Noise Ratio

Since the physics behind signal excitation is the same for any type of coil and are easily explained using loop coils it makes sense to describe signal excitation via loop coils. Signal excitation is based on the Biot-Savart law; which describes the magnetic flux density generated by an electrical current. The magnetic flux density, B (or more commonly noted in MR as the transmit magnetic field, B_1^+) at any given point in space, produced by a short segment of wire $d\mathbf{l}$ is directly proportional to the current, I, on the wire:

$$\mathbf{B} = \frac{\mu_0}{4\pi} \int_C \frac{I d\mathbf{l} \times \mathbf{r}}{|\mathbf{r}|^3} \tag{69}$$

where the direction of $d\mathbf{l}$ is in the direction of the current and where the vector $\mathbf{r}$ points for the short segment of current to the observation point where the magnetic field is computed. μ_O is the magnetic permeability in a vacuum ($4\pi 10^{-7}$ Tm/A). Figure 5 shows the Biot-Savart law for a loop coil.

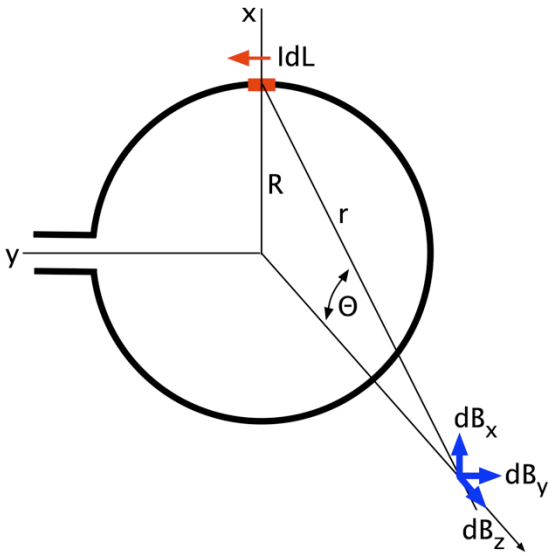

Figure 5: Biot-Savart Law for a loop of wire.

During reception, the signal detected in the coil is the emf, ξ, induced in it by the precessing sample magnetization, M_t is

$$\begin{aligned}\xi &= -\frac{d}{dt}\Phi_M \\ &= -\int_{sample}\frac{\partial}{\partial t}\mathbf{B}_1^- \cdot \mathbf{M}_t dV\end{aligned} \tag{70}$$

where $\mathbf{B}_1^-$ is the receptive field of the coil. Ignoring the phase, if receive field is homogeneous over the sample volume the induced emf signal is

$$\xi = \omega_O B_1^- M_t V_S \tag{71}$$

The noise voltage in the coil is

$$N = \sqrt{4k_B T \Delta f R} \tag{72}$$

where k_B is the Boltzmann's constant, T is the temperature, R is the sum resistance of the coil, the electronics and sample and Δf is the bandwidth.

The signal to noise ratio (SNR) in a single, uncoupled coil is:

$$SNR = \frac{\xi}{N} = \frac{\omega_O B_1^- M_t V_S}{\sqrt{4 k_B T \Delta f R}} \tag{73}$$

2.5 Coupling and Decoupling Methods

Coupling is the transferring of signal between any two coils; this will only occur within an array. Coupling in this context is the coupling of noise signal between any two coils. Coupling can either be resistive (E-field coupling) or inductive (H-field coupling). While restive coupling does occur, the primary concern in designing RF coils for MR imaging is inductive coupling. Inductive coupling results in resonant peak splitting and loss of sensitivity at the resonant frequency. To better understand the noise coupling, two coils are shown in figure 6. Here, the inductive coupling, M between two coils equal to the mutual inductive coupling constant, k, and the inductance in the coil.

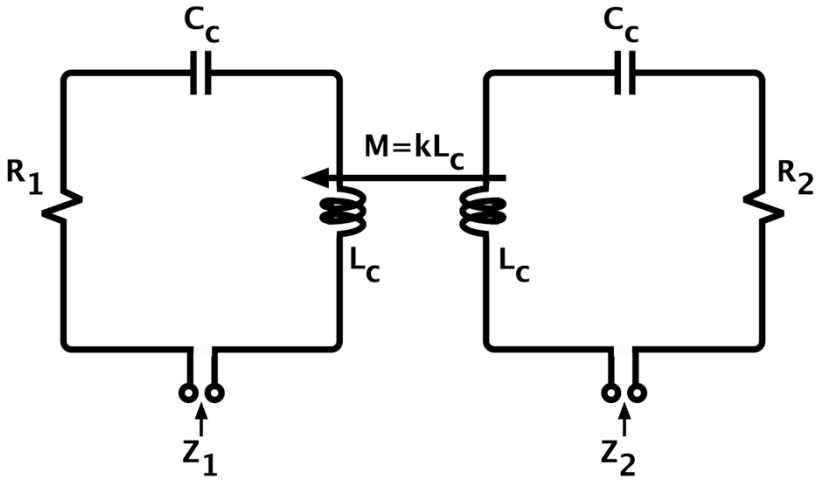

Figure 6: Inductive Coupling between two coils. The coupling, M, is equal to the coupling constant times the coil's inductance.

There are two main affects of inductive coupling. The first is changing the input impedance of the coil. Earlier, the impedance of the coil at resonance was equal to the resistance in the coil. Now, due to the inductive coupling the impedance of coil 1 in figure 2 is

$$Z_{IN} = R_1 + \frac{\omega_O^2 M_t^2}{Z_2} \tag{74}$$

The second and more important change due to coupling is the loss in SNR. Since SNR is dependant on the coil impedance, changing, and increasing the coil's impedance will reduce the SNR. The SNR between two coupled coils is now

$$SNR_1 = \frac{\omega_O B_1^- M_t V_S}{\sqrt{4 k_B T \Delta f \left(R_1 + \frac{\omega_O^2 M_t^2}{Z_2} \right)}} \tag{75}$$

From equation 13, as the mutual inductance between the two coils approaches zero, or if the impedance of the second coil approaches infinity equation 13 reduces to equation 11.

There are three common methods to reduce coupling between coils within an array.

The first is through geometric overlap. Geometric overlap, as shown in figure 7 forces the magnetic flux between the two coils to zero. It works because, at a certain amount of overlap, the total magnetic flux density through the overlapped regions of the two coils is greater then the flux density through the non-overlapped regions. Therefore the total magnetic flux passing either coil cancels. The amount of overlap required can be determined analytically by Faraday's Law of induction, (equation 8). As a rule of thumb however, the center of circular loop coils should be separated by 0.75 times their

diameters and the centers of square loop coils should be separated by 0.9 times their side lengths.

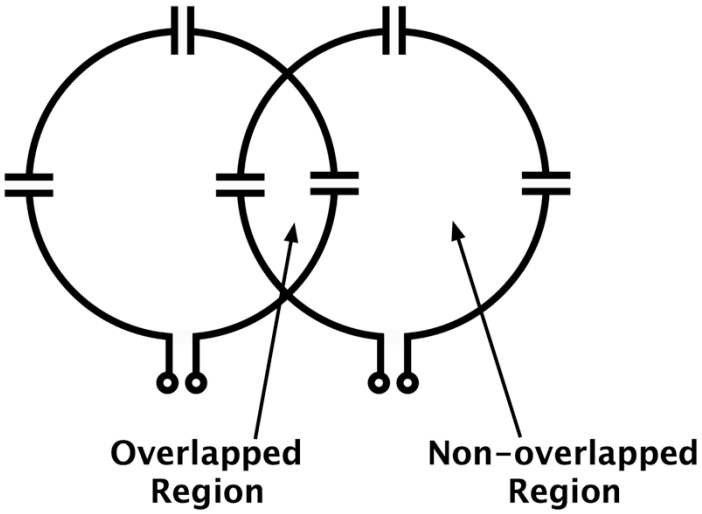

Figure 7: Overlapping of two coils to reduce or eliminate the mutual inductance between the two.

A second method for decoupling loop coils within an array is through capacitive decoupling. When two coils are coupled, the mutual inductance (Z_3) between the two coils will be:

$$Z_3 = R_3 + j\omega M \tag{76}$$

Where R_3 is the resistive coupling between the two coils and jωM is the inductive coupling between both coils. By inserting a capacitor, C, the mutual impedance becomes

$$Z_3 = R_3 + j\omega_O M - j\frac{1}{\omega_O C} \tag{77}$$

To eliminate the inductive coupling the capacitor's value should be

$$C = \frac{1}{\omega^2 M} \tag{78}$$

This will reduce the mutual impedance between both coils to only the resistive coupling, which is usually small and can often be ignored.

The final most common method for decoupling receive-only coils is through preamplifier decoupling. Originally was limited to only low-impedance preamplifiers, but now has been expanded to any low-noise amplifiers (LNA).

Figure 8 shows the general concept for both matching and decoupling of receive-only coils using low-noise preamplifiers. Starting from the right, the preamplifier is designed to provide adequate gain and optimal noise performance when attached to a 50Ω source. The preamplifier is attached to the phase shifter, usually a coaxial cable; the purpose of the phase shifter is to transform complex input impedance of the preamplifier to resistance, R_s, which is close to a short circuit. The phase shifter is attached to a loaded coil tuned to resonate at the Larmor frequency with a matching network. The matching network will transform the complex impedance of the coil to 50Ω real and provide a λ/4 phase shift. The purpose of the λ/4 phase shift is to transform the low impedance, R_S, into a large resistance, R_O, seen at the coil terminals. The large impedance at the coil terminal will block current flowing through the coil, thus preventing coupling, while allowing the MR voltage signal induced in the coil to be transferred to the preamplifier. It should be noted that the phase shifter will not change the 50Ω impedance seen by the preamplifier; it will only change the phase. Furthermore, changing the amount of phase added by the phase shifter will not affect the coil impedance as it is seen by the preamplifier but it will change the preamplifier impedance as it is seen at the coil terminals. If the input impedance of the preamplifier is already near R_S, the phase shifter is unnecessary.

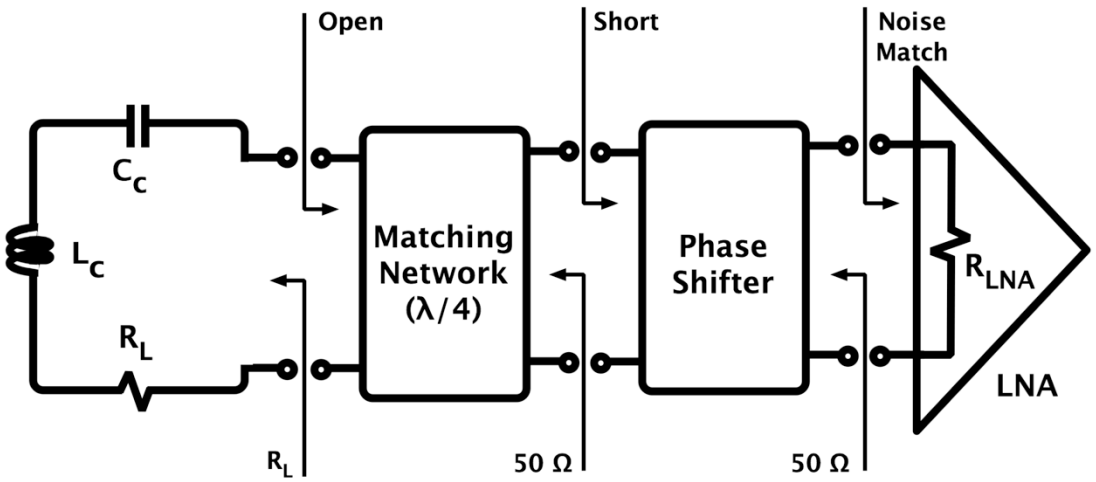

Figure 8: Accepted method to tune, match, a receive-only coil using a low noise amplifier (LNA). This method will also reduce current in the coil, decoupling it from neighboring coils. Here, the LNA is noise matched to provide the greatest SNR possible when attached to a 50Ω source. The phase shifter is designed to transform the input impedance of the LNA to a low impedance. The phase shifter is attached to the loaded coil with a matching network. The matching network should also have a λ/4 phase shift, this phase shift will transform the low impedance at the phase shifter to high impedance and the coil terminals. If the LNA already has a low input-impedance, the phase shifter is not necessary.

3 TEM Resonators and Arrays

TEM coils are any type of resonators that support a TEM wave; the most common type TEM coil is the microstrip(1-4). It consists of a center conductor, with width w_c, which is separated from the ground plate, with width w_g by a dielectric of height h. The dielectric between the center and ground conductor has a relative permittivity (or "dielectric constant") ε_r. The overall resonator length is l. Both the center conductor and the ground plate have a certain thickness, t; however, it is assumed to be negligible ($t/h < 0.005$). Figure 6 shows the TEM resonator.

The electric and magnetic fields (E- and H-fields respectively) of a microstrip coil propagating a TEM wave is shown in figure 9. The sketch of the field lines shows that the majority of the E-field is localized inside the dielectric while the H-field propagates beyond, outside of the strip. If the relative permittivity of the dielectric is greater the 1, then the microstrip will, strictly speaking, propagate a quasi-TEM mode. The quasi-TEM mode, or hybrid TM-TE mode propagation occurs because the phase velocity above the center conductor, in free space, will be the speed of light, c, whereas the phase velocity below the center conductor, in the dielectric, will be $c/\sqrt{\varepsilon_r}$. This discontinuity in the phase velocity between free space and the dielectric can create longitudinal E- and H-fields, ($E_z \neq 0$; $H_z \neq 0$). Usually these longitudinal fields are small relative to the transverse fields and the overall phase velocity of the microstrip is $c/\sqrt{\varepsilon_e}$ where ε_e can be approximated as:

$$\varepsilon_e = \frac{\varepsilon_r + 1}{2} + \frac{\varepsilon_r - 1}{2}\left(\frac{1}{\sqrt{1+12\left(h/w_c\right)}}\right) \tag{79}$$

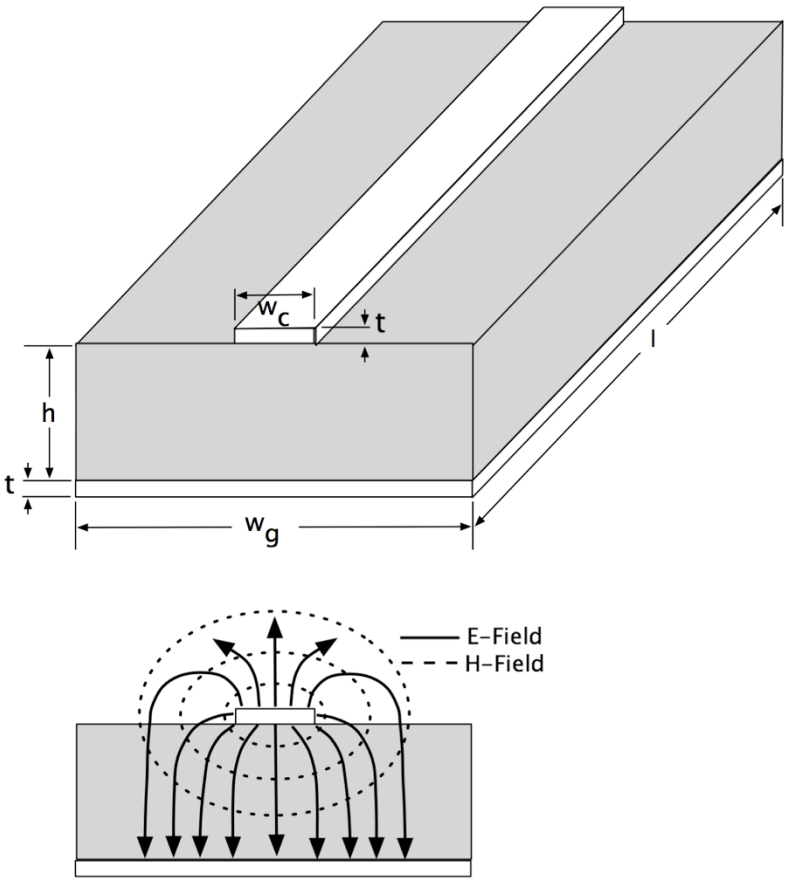

Figure 9: The dimensions and the E- and H-field of the standard TEM resonator. The TEM resonator is composed of a center conductor, with width, w_C, and a ground plate conductor of width, w_g separated by a dielectric of height, h. The resonator has length, l. In (b) it is noticed that most of the E-field stays within the dielectric while the H-field is present in both the dielectric and in free space.

3.1 Characteristic Impedance

Microstrip resonators can only propagate a TEM or quasi-TEM mode when the characteristic impedance, Z_o, is between 20 and 120Ω. Impedances lower then this propagates higher-order modes, and impedances higher this in MRI coils, will most likely violate the microstrip assumption that the transverse dimensions are much less then half the wavelength in the dielectric. The characteristic impedance of a microstrip is:

$$Z_0 = \frac{60}{\sqrt{\varepsilon_e}} \ln\left(8\frac{h}{w_c} + \frac{w_c}{4h}\right) \qquad \text{when } w_c/h < 1 \qquad (80)$$

or:

$$Z_o = \frac{120}{\sqrt{\varepsilon_e}\left[\frac{w_c}{h} + 1.393 + \frac{2}{3}\ln\left(\frac{w_c}{h} + 1.44\right)\right]} \qquad \text{when } w_c/h > 1 \qquad (81)$$

3.2 Resonance Condition

As with the loop coil, in order to achieve the resonance condition the average stored magnetic energy and the electric energies are equal. This occurs naturally when a microstrip is either λ/4 or λ/2 in length and can either be open- or short-circuited. Practically, a λ/2 open-circuit resonator provides the greatest B_1 field and sensitivity at the center of the coil and is therefore predominantly used for all MR imaging and spectroscopy. λ/4 and short-circuited resonators are only be employed when an asymmetric field is wanted or necessary.

While Lee(5,6) has previously shown the use of true λ/2 microstrip resonators, their long lengths (~2.35m at 1.5T or 0.5m at 7T with an ε_r=1) are impractical to implement.

Use of dielectrics with high relative permittivity have been proposed, to reduce the electrical length of microstrip resonators, but a more practical method is capacitively shunting the microstrip. From here, it is assumed that that all TEM resonators are capacitively shunted.

The input impedance of the capacitively shunted microstrip is

$$Z_{IN} = \frac{X_{C_1} Z_0 \left(X_{C_2} + jZ_0 \tan(\beta l) \right)}{Z_0 \left(X_{C_1} + X_{C_2} \right) + j \left(X_{C_1} X_{C_2} + Z_0^2 \right) \tan(\beta l)} \tag{82}$$

where $X_{C1} = 1/j\omega C_1$, $X_{C2} = 1/j\omega C_2$ and β is the phase constant

$$\beta = \frac{\omega_0 \sqrt{\varepsilon_e}}{c} \tag{83}$$

c is the speed of light.

In the case of the microstrip resonator, both discrete capacitors should be equivalent, ($X_{C1}=X_{C2}$ and $C_T=C_1=C_2$). Different capacitive values will lead to an asymmetric magnetic field along the length of the resonator, with the region of the greatest magnetic field strength being shifted towards the capacitor with the lower impedance.

By applying the resonant condition of a parallel resonant circuit to equation 20, the capacitance of the two shunt tuning capacitors, C_T, for a microstrip of a given length and phase velocity is

$$C_T = \frac{\cos(\beta l) + 1}{\omega_0 Z_0 \sin(\beta l)} \tag{84}$$

3.3 Quality Factor

The unloaded quality factor, Q_u, of the transmission line resonators is

$$Q_u = \frac{\pi}{2\alpha l} \tag{85}$$

where α is the attenuation constant due to losses in dielectric, α_d, and the conductor, α_c,

$$\alpha = \alpha_d + \alpha_c = \frac{k_0 \varepsilon_r \left(\varepsilon_e - 1\right) \tan\delta}{2\sqrt{\varepsilon}_e \left(\varepsilon_r - 1\right)} + \frac{R_S}{Z_0 w_C} \tag{86}$$

where k_0 is the radial wave number, tan δ is the loss tangent of the dielectric and R_s is the surface resistivity of the conductor.

The loaded quality factor, Q_L, of the transmission line resonators is

$$Q_L = \frac{\pi}{2\alpha l + R_L} \tag{87}$$

where R_L represents the losses of the load.

3.4 TEM Coil Coupling and Decoupling

Owing to its complexity, an analytical closed form solution for the mutual inductance and capacitance between two microstrip resonators, based on physical dimensions, is beyond the scope of this article. The full analytical solution for the mutual inductance and capacitance between coupled microstrips is described by Gupta *et al* (7). As with any array, decoupling TEM coils within an array is important for B_1 shimming, increased SNR, possibly decreased SAR, and improved image homogeneity. Owing to the smaller width of the TEM element (when compared to loop elements), these coils can be packed tightly together, which also increases coupling. In addition, because of their topography, means of decoupling remain limited, with capacitive decoupling being predominant. Fortunately, although there are several proven methods of capacitive decoupling that can provide excellent decoupling for a given load, for moderately coupled TEM elements a single decoupling capacitor bridging the neighboring elements is sufficient. As with loop

arrays, the reactive impedance of the decoupling capacitors is same as equation 16. However, when the isolation between two neighboring elements is less than 12 db, more aggressive decoupling strategies are usually required. In this case, a second decoupling capacitor bridging the two neighboring ground plates is required. Here, the two capacitors are tuned in concert to provide the greatest decoupling possible.

Using a distributed capacitor along the ground plate has recently been suggested as a novel method for decoupling TEM elements. This method is elegant because it simultaneously creates a continuous RF shield along the ground plate while decoupling two neighboring elements; however, it can be problematic to construct. Small changes to the physical geometry of the distributed capacitor can create significant changes in the impedance between the two neighboring elements. Therefore, it is important to have a good understanding of the loading conditions a priori before installing this decoupling method. Decoupling capacitors are lossy, and can create parasitic current loops and field perturbing loops, potentially destroying the desired field profile of the coil; therefore, the least amount of decoupling possible to achieve greater than 18 dB of isolation between nearest neighbor channels was used. Finally, during transmit, due to the B_1^+ shim, significant current and voltage drops across the decoupling capacitors are possible, the magnitude and distribution of which can vary with B_1^+ shimming. Depending on the phase set, following B_1^+ shimming, it is possible that the voltage drop across the decoupling capacitor can be nearly twice the output voltage of the amplifiers, with the current through the capacitor being proportional to reactive impedance of the capacitor. This needs to be considered when determining the appropriate power rating of the

decoupling capacitors.

3.5 Microstrip Optimization

Mircostrip resonator optimization, similar to that of any other array, is highly dependent on the application and the field strength in which the array will be used. However, with that being said, there are several known parameters that affect the performance of the microstrip resonator regardless of application or field strength. The three most frequently adjusted parameters for microstrip optimization are the dielectric height (h), dielectric permittivity or constant (ε_r), and the conductor width (wc). The length (l) of the array is also considered in optimization studies and while it does influence the performance of the array, in practice, the length of the array is often determined by the dielectric used and the fleld of view necessary for the application. The length of the array should not be longer than necessary, especially at ultra-high field strengths, as the extra inductance adds to radiative losses and reduces the self-resonance frequency of the resonator. A fourth parameter that is very rarely considered but can have significant consequences to the microstrip design is the ground plate.

Dielectric Height

Figure 5(b) shows the field lines for a microstrip resonator and explains how the dielectric height affects the behavior of the coil. If the dielectric height between the center conductor and the group plate is very narrow, the field will be concentrated and confined near the coil, creating a strong B_1 field very close to the coil, but it drops off

rapidly. Conversely, a microstrip resonator with a wide dielectric height will not confine the B_1 field as much and will allow for greater penetration of the B_1 field into the sample, but have less sensitivity near the coil.

Relative Permittivity

Dielectrics with low relative permittivity should be preferred over dielectrics with high relative permittivity; optimizations of single element microstrip resonators at low field strengths have shown that air ($\varepsilon_r = 1$) yields the highest SNR. Dielectrics with high permittivities should only be used when it is necessary to reduce the circuit length. They can also be used to reduce the coupling between TEM elements in an array. Regardless of the permittivity of the dielectric, it is crucial that the dielectric does not have a high loss tangent (δ).

Center Conductor Width

Optimizing the center conductor width is similar to optimizing the dielectric height, in that there are compromises involved in choosing a narrow strip over a thick strip. A thin, narrow conductor strip generates a very strong B_1 field near the conductor, but the field falls off rapidly and consequentially does not couple to the sample very well. Wider strips generate a weaker B1 near the coil but couple better to the sample.

Recently, interesting work has been performed on changing the strip's impedance by changing its physical geometry in order to improve both the penetration and homogeneity of the profile(8).

Ground Plate

The ground plate, which is usually a forgotten parameter, is essential to an efficient microstrip array. If designed incorrectly, the ground plate can decrease the transmit efficiency, perturb and reduce the B1 fields, generate eddy currents, and increase mutual inductance between resonators. To avoid this, the ground plate needs to be sufficiently wide (wg $\ll$ wc and wc $\ll$ h) such that it does not perturb the field lines. If the ground plate width is too narrow, the resonator will perform more like a parallel plate resonator or a two-wire loop. In addition, if the ground plate is too narrow or discontinuous, there will be RF "leakage" behind the resonator, which can lead to reduced efficiency and possible image artifacts.

Conversely, an RF ground plate that is too wide may increase eddy currents during the imaging experiment; a double-sided slotted shield is the best way to compensate for this. The ground plate should be thicker than 2 skin depths at the frequency of interest to reduce resistive losses in the resonator, but not thicker than 5 skin depths as it increases the risk of eddy currents. The individual microstrip resonator is the building block of a microstrip array, and once the individual coil is optimized for the specific application, it can be replicated into an array. Just as the individual coils have parameters that need to be optimized, the array also has parameters that need to be optimized.

4. INITIAL RESULTS OF CARDIAC IMAGING AT 7 T

Originally published in *Magnetic Resonance in Medicine,* 2009, 61(3): 517-524.

Carl J. Snyder, Lance DelaBarre, Greg J. Metzger, Pierre-Francois van de Moortele, Can Akgun, Kamil Ugurbil, J. Thomas Vaughan

ABSTRACT

This work reports preliminary results from the first human cardiac imaging at 7 T. Images were acquired using an 8-channel transmission line (TEM) array together with local B_1 shimming. The TEM array consisted of anterior and posterior plates closely positioned to the subjects' thorax. The currents in the independent elements of these arrays were phased to promote constructive interference of the complex, short wavelength RF field over the entire heart. Anatomic and functional images were acquired within a single breath hold to reduce respiratory motion artifacts while a vector cardiogram (VCG) was employed to mitigate cardiac motion artifacts and gating. SAR exposure was modeled, monitored and was limited to FDA guidelines for the human torso in subject studies. Preliminary results including short-axis and four-chamber VCG-retrogated FLASH cines, as well as, short-axis TSE images demonstrate the feasibility of safe and accurate human cardiac imaging at 7 T.

Key Words: Cardiac Imaging; Ultra-High Field; Transmit/Receive Arrays; B_1 Shimming

4.1 INTRODUCTION

Cardiovascular magnetic resonance (CMR) imaging has rapidly evolved as an important tool in the arsenal of techniques employed for the management of cardiovascular disease (9-12). This is largely based on developments in real time imaging(13,14), imaging of myocardial perfusion at rest and under pharmacological stress (10,15) and assessment of regional wall motion(16). However, in other areas critical to diagnosis of cardiac disease, such as coronary artery angiography, MR methods (17-19)remain suboptimal despite continuous improvements over the years, due primarily to low signal-to-noise ratios (SNR)(19). Similarly, while animal studies have indicated the great potential of ^{31}P spectroscopy to investigate *in vivo* energetics in the myocardium(20,21) studies in the human heart are again limited due to low SNR(22,23).

Since SNR is approximately proportional to field strength, increasing magnetic fields can alleviate SNR limitations. Results from 3 T have shown some promise when compared to 1.5 T (24,25) due to increased SNR and contrast to noise ratio (CNR). These studies, however, have also highlighted the challenges of working at elevated magnetic fields, such as decreased T_2^* times, increased B_0 inhomogeneities due to magnetic susceptibility effects, non-uniform B_1 distribution, increased RF deposition, and the degradation of the electrocardiogram (ECG) as a result of increased magneto-hydrodynamic (MHD) effects. Particularly, the non-uniformities in B_1 become a real challenge with increasing field strength beyond 3 Tesla, as the radio frequency (RF) wavelength becomes smaller than the size of the imaged object. Potential solutions to this problem, however, have been recently demonstrated for applications in the head

(3,26,27) and even more recently for prostate imaging at 7 T (28). Consequently, while it was virtually unthinkable to pursue imaging in the human chest at 7 tesla in the past, these new developments suggest that the problem may be tractable. Accordingly, the objective of this investigation was to use and build on some of these developments in order to investigate the feasibility of safe and successful cardiac imaging at 7 tesla.

4.2 METHODS

An eight-channel TEM transceiver was used together with B_1 shimming localized in the heart (29). SAR levels in the torso were predicted from models and average SAR was monitored during studies to assure subject safety. VCG-retrogated FLASH cine protocols and VCG-gated turbo-spin echo (TSE) sequences were used to image the heart along both the short and four-chambered axes. A more detailed account of the materials and methods follows.

RF coil and hardware

An eight-channel, flexible, transceiver array (Fig. 10a) was built according to stripline transmission line (TEM) principles (1,3,30). This eight-channel array consisted of a pair of four-element arrays, one located anterior and the other posterior to the chest (Fig. 10b). Four coil elements were attached in a parallel configuration to a flexible polytetrafluoroethylene (PTFE) plate measuring 22.7 cm x 35.6 cm x 0.3 cm for both the anterior and posterior plates. The individual coil elements were 15.3 cm long with a 1.27-cm wide inner conductor and a 5.0-cm wide outer conductor, separated by a 1.9-cm

thick bar of PTFE, a dielectric with a low loss tangent and a permittivity of 2.08. A 5.0-cm air gap separated the outer conductor of each coil element.

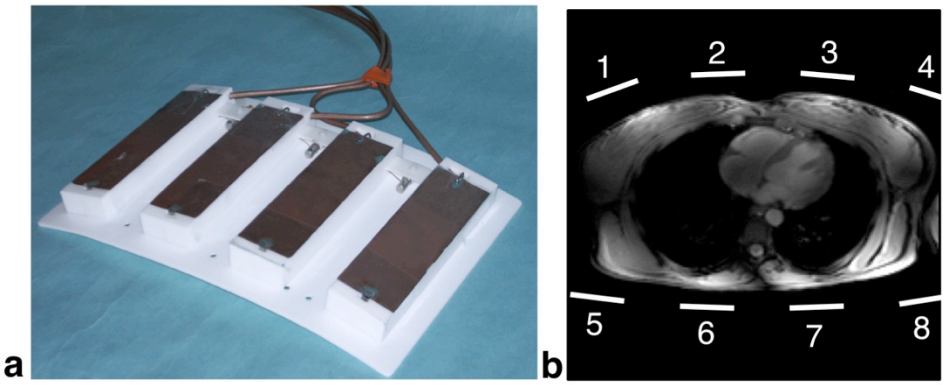

Figure 10: Half of the eight channel TEM array used for cardiac imaging. **(b)** Axial FLASH image showing the approximate placement of the eight channels.

Each element was individually tuned to 297 MHz (7 T), and matched to a 50-Ω, coaxial signal line. Capacitive decoupling facilitated greater than 18 dB isolation between elements. All bench measurements required for coil tuning, matching, isolation and other circuit characterizations were performed using a calibrated Hewlett-Packard (Palo Alto, CA) HP 4396A network analyzer together with an HP 85046A "S" parameter test set.

Imaging experiments were performed on a 7 T (ω_o = 297.14 MHz) magnet (Magnex Scientific, UK) interfaced to a Siemens console. Siemens Avanto whole body gradients were set to a slew rate of 170 T m^{-1} s^{-1} and a maximum amplitude of 40 m mT^{-1}. The output of an 8 kW RF power amplifier (Communications Power Corp., Hauppauge, NY) was divided into eight channels with equal magnitude and phase through an 8-way RF

splitter (Werlatone, Brewster, NY) to feed the eight element coils. Eight high-power phase shifters (Advanced Technical Materials, Inc., Patchogue, NY) and incremental cable lengths were used to adjust the transmit phase of each transmit coil as required to accomplish B_1 shimming for optimal image homogeneity over the heart. Power divider specifications included -0.4 dB insertion loss and 1° phase resolution, while the phase shifters measured -0.5 dB insertion loss over a phase range of 120° at 297 MHz.

B_1^+ shimming

For a given location in space, the maximum efficiency of a transmit array will occur when there is complete phase coherence between all channel's B_1^+ vectors. In this case, the magnitude of sum of the complex B_1^+ vectors, which we refer to as the "available B_1^+", equals the sum of their magnitudes. Opposite to this case, when B_1^+ vectors are not in phase coherence, the effective B_1^+, which corresponds to the magnitude of sum of complex B_1^+ vectors, will only amount to a fraction of the available B_1^+ due to complex destructive interferences (27).

To optimize the RF transmit efficiency over the heart, the transmit B_1 field (B_1^+) components of the independent coil elements were adjusted, or "shimmed", to affect an approximate phase coherence or "constructive interference" of the short RF wavelengths (12 cm) over the region of interest (26-28,31). In order to perform such B_1 optimization, calibration scans were first obtained to determine relative transmit B_1 maps for each transmit coil, as described in. Based on those relative B_1 maps, we then perform a modified version of a local B_1 phase shimming technique which has been demonstrated

in the head and in the prostate at ultra-high fields (26-28,31). A brief description of those methods follows.

Calibration scans obtained to map the relative excitation profiles consist in a series of low resolution, low flip angle gradient echo images. Each image is collected when transmitting through only one array element at a time, while all other transmit elements are terminated on 50 Ω. Relative transmit B_1^+ phases are then calculated based on those images. It is also possible with the same image series, and without knowing the absolute magnitude of B_1^+, to estimate for each pixel which fraction of the available B_1^+ is obtained for a given set of transmit coil phases (27,28). This approximation relies on two conditions: a low excitation flip angle in order to have an approximately linear relationship between B_1^+ and the actual flip angle (with $\sin(\theta) \sim= \theta$ for $\theta<10°$), and minimal T_1 weighting in the resulting images.

From the gradient echo image series, a Sum of Magnitude (SOM) image can be written as:

$$SOM = \sum_{J=1}^{N} \sum_{K=1}^{M} \left| \mathbf{p}_{J,K} \right|, \tag{88}$$

where **p** is the complex valued signal in a pixel, K is the index of transmit channels (K=1,2,…,M) and J is the index of receiver channels (J=1,2,…,N). For any given set of phases, β_K, the result that would occur when pulsing all coils simultaneously can be simulated numerically by applying those phases to the complex images and then computing a Magnitude of Sum (MOS) image:

$$MOS = \sum_{J=1}^{N} \left| \sum_{K=1}^{M} \left(p_{J,K} \cdot e^{-i\beta_K} \right) \right|. \tag{89}$$

The ratio of MOS to SOM for a given β_K predict for each pixel the fraction of available B_1^+ actually obtained when experimentally transmitting with all channels simultaneously. For a small sized target, it is possible to calculate a set of phases β_K yielding transmit phase coherence through all channels within the target, resulting in very high local transmit efficiency. Successful local B_1 shimming based on this approach has been demonstrated in the prostate (28) at ultra high field.

While the aforementioned technique works well for shimming over the entire prostate, it does not work well for shimming over the entire heart; this is mainly due to the size of the heart and its asymmetric placement with respect to the array. These two conditions result in large variations of transmit B_1 phase and amplitude for each coil within the heart. Ideally, B_1 shimming calculations over such large ROI's should be based on complex B_1^+ profile (magnitude and phase) of each transmitting coil. However, obtaining magnitude B_1^+ map for each of the eight transmit channels would take an extensive time during a volunteer session. Therefore, a modified version of the local B_1 phase shimming algorithm was implemented, which is referred to as "local phase, and magnitude-approximation B_1^+ shimming". Instead of utilizing actual magnitude B_1^+ profiles, this approach utilizes the magnitude of the images series obtained with one coil transmitting at a time, merged with the calculated relative transmit B_1^+ phases (we refer to those hybrid images as "approximation B_1^+ maps"). The modified algorithm consists in a non linear minimization problem which incorporates each pixel in the ROI. The minimization criteria is:

$$\arg\min_{\beta_K \in [0,2\pi]} \frac{std(F(\beta_K))}{\left(mean(F(\beta_K))\right)^2}, \tag{90}$$

where $F(\beta_K)$ is the magnitude of the sum of the approximate B_1^+ maps with, for a given β_K:

$$F(\beta_K) = \left| \sum_{K=1}^{M} B^{+}_{1,K\,app} \cdot e^{-i\beta_K} \right|, \tag{91}$$

with $B^{+}_{1,K_{app}}$ being the approximation B_1^+ map for each transmit coil K. The minimization critera given in Eq. 3 was determined empirically and favors increased transmit efficiency over homogeneity. A global optimization, which avoids local minima, was computed using a Multilevel Coordinate Search (32) to solve for the phases of the individual transmit elements.

To determine the improvement in transmit efficiency, due to the B_1^+ shimming, the predicted relative transmit efficiency (RTE) and estimated B_1^+ nonuniformity were calculated from combinations of the approximated B_1^+ maps with different phase sets (28).

SAR modeling

Remcom's Finite Difference Time Domain software (XFDTD, Remcom, Inc., State College, PA) was used for numerical modeling of SAR before and after B_1 shimming was performed.

The complex electric field maps (E) were also solved for each transmit channel. The resulting complex E field components (E_x, E_y, and E_z) were determined by summing the E-field maps after applying the corresponding RF phases for each phase set (equal phase or local B_1^+ phase shim). SAR was calculated in accordance to the standard formula,

$$SAR \propto \frac{\rho}{\sigma}\left(\left|\vec{E}_x\right|^2 + \left|\vec{E}_y\right|^2 + \left|\vec{E}_z\right|^2 \right), \tag{92}$$

where ρ is the proton density and σ is tissue conductivity. The ratio of the average B_1^+ magnitude of the equal phase condition to the local B_1^+ phase shim was calculated. The square of this ratio was used to rescale the SAR maps.

Cardiac image acquisition

Volunteers were recruited and imaged under a protocol approved by the University of Minnesota's Institutional Review Board. For all imaging experiments, subjects were supine with the two halves of the transceiver coil placed anterior and posterior to the chest wall. For additional comfort, the volunteers were insulated from the array by a 1.3 cm thick, closed-cell foam pad. All images were acquired during a breath hold to reduce respiratory motion artifacts while the Siemens' VCG was used to gate image acquisition.

Low-resolution, multi-slice, gradient echo scout images were first acquired with the following parameters: TR/TE =7.1 ms/2.05 ms; matrix = 192 x 192; FOV = 40.0 cm x 40.0 cm, slice thickness = 0.5 cm. To map the relative excitation phase and approximate magnitude in the body generated by each coil element, a series of eight cardiac gated, low resolution, low flip angle gradient echo images were acquired. The image parameters were: TR/TE = 11.54 ms/4.1 ms; Matrix=192 x 122; FOV=40.0 cm x 40.0 cm; slice thickness=0.5 cm. The short repetition time was used in order to acquire all the calibration data in a single breath hold. While the amount of T_1 weighting is spatially varying across the heart, it is expected to be minimal in these data due to the extremely low power used and the distance the heart is from the coil elements when used individually for RF transmission. Each image was collected by transmitting with only

one array element at a time, while the other array elements were properly terminated on the RF power amplifier input port of each channels' transmit/receive switch. All eight transceive coils were used simultaneously during reception, and the corresponding signals were sampled on eight receiver channels of the Siemens console. Following localized B_1^+ shimming based on the previous data, transverse, short axis and four-chamber views were acquired with VCG-retrogated FLASH cines: TR/TE = 6.1 ms / 3.06 ms; matrix = 192 x 132; FOV = 34.0 cm x 23.0 cm; slice thickness = 0.5 cm. Sixty successive phases of the cardiac cycle were interpolated from data acquired over the course of 12 heartbeats.

FLASH cines were acquired for three different shim configurations: 1) all coil elements in both halves of the array set to equal transmit phase (equal phase), 2) elements in the anterior half set in 180° phase opposition with the posterior half (opposite phase) and 3) coil element phases adjusted to optimize the local B_1^+ in the heart based on experimentally measured B_1^+ phases for each array element for each individual subject (B_1 shimmed). These cines were used to evaluate the effectiveness of shimming the B_1 field over a local ROI around the heart.

Additionally, TSE images were acquired along the short axis (TR/TE = 909.7 ms/45.0 ms; matrix = 192 x 156; FOV = 34.0 cm x 23.0 cm; slice thickness = 0.5 cm, ETL = 9; NEX = 2; iPAT = 2 with 26 reference lines). Refocusing was achieved with a nominal 180° pulse and Siemen's standard weak fat saturation preparation pulse was employed. Normalization filters were applied for image intensity correction.

It should be mentioned that standard pre-scan calibration routines supplied by manufacturers for clinical use are not accurate for ultra-high field cardiac imaging experiments. For example, the standard power calibration strategy which integrates signal over an entire transverse slice at iso-center works well for clinical field strengths but is not appropriate for 7 T imaging of the body because of the increasingly inhomogeneous B_1^+ (33). Therefore, in this study, the transmit power was incrementally increased to find power levels that maximized contrast and signal homogeneity.

SNR measurements

SNR was calculated for three different shim configurations listed above: equal phases, opposite phases, and B_1 shimmed. Signal levels were computed from single time-frame images, during systole, from the short axis FLASH cines by drawing an oblique line plot across the entire chest. Noise levels were computed by determining the standard deviation of the signal intensity in identical images acquired without applying transmit RF power.

4.3 RESULTS AND DISCUSSION

All volunteers were given exit interviews regarding their experience during the 7 T cardiac exam; three of the volunteers commented on “sleepiness”, two reported “metallic tastes” and one note each was recorded for feeling “warm” and “cold.”

Experimentally, it was found that reversing the RL and LL VCG leads had the greatest impact on increasing the R wave with respect to the MHD effect in the scanner; this modification to the standard VCG placement provided the most reliable method for

accurate cardiac gating and VCG triggering. The VCG traces from outside and within the magnet are shown in Figure 11 with the RL and LL leads reversed. While MHD distortion of the VCG signal from within the magnet is apparent; the accentuated T waves do not preclude accurate and effective cardiac monitoring or gating as indicated by the red arrows positioned above the appropriate QRS complex.

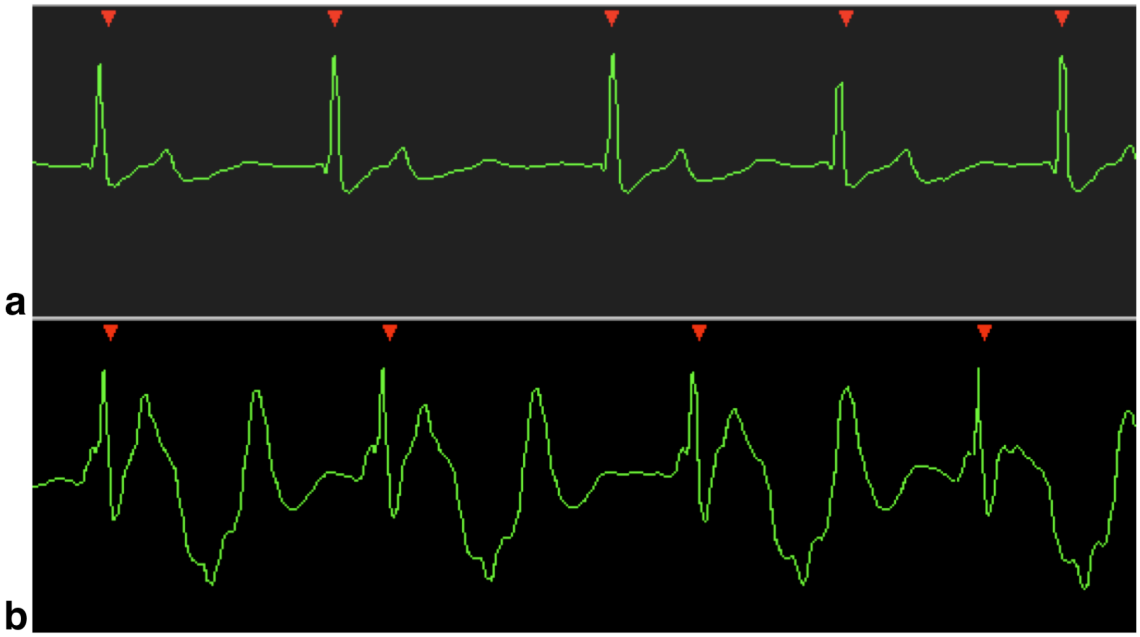

Figure 11: Vector cardiogram traces of the aV_F channel acquired **(a)** outside (approximately 0.5 T) and **(b)** inside the 7 T whole body magnet. The red arrows show the accuracy of the gating in spite of the severe magneto-hydrodynamic effect.

B_1 Shimming

Experimentally attained MOS/SOM maps are shown in Figure 12 for the same transmit power with equal phases across all transmit channels (Fig 12a) and after subject specific B_1^+ shimming (Fig 12c). The maximal attainable B_1^+ in a given voxel is defined as the B_1^+ that would be achieved if in that voxel the contribution of each coil array element would be in-phase and thus add constructively. In Figure 12a, approximately

only 20% of the B_1^+ field in the heart adds constructively, as opposed to approximately 66% for the B_1^+ shimmed case in 12c. Figures 12b and 12d show the gradient echo image before and after shimming, respectively. For the example shown in Figure 12, the optimal phases obtained for this subject for the different elements of the array coil were determined to be 146, 38, 0, 61 degrees for coils 1 through four, respectively, and 75, 346, 210, 208 degrees for coils 5 through 8 respectively.

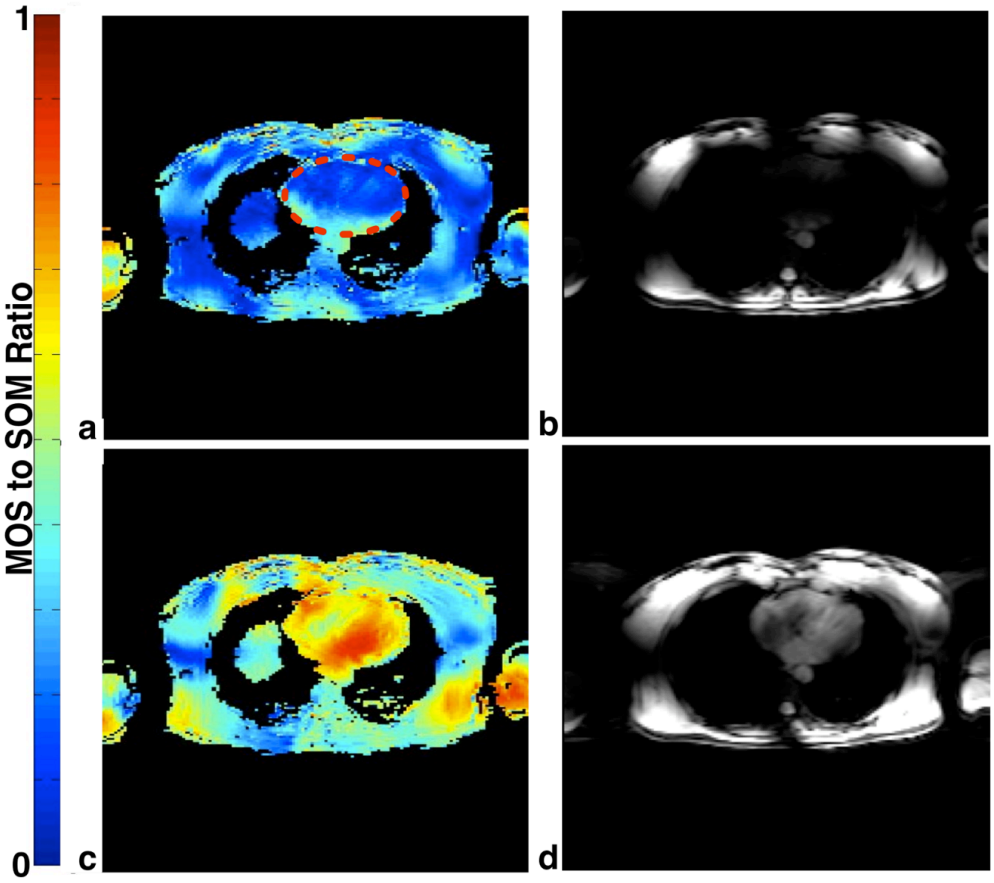

Figure 12: Available B_1^+ field are predicted for **(a)** equal phased current elements and and **(c)** optimally phased current elements for the heart region, given the same RF transmit pulse. **(b)** and **(d)** show the low resolution GRE images for cases (a) and (c) respectively. Available B_1^+ is normalized to 1 if in a voxel all the individual B_1^+ vectors generated by each coil array element are in phase add constructively.

The predicted RTE (28) is the ratio of the MOS after B_1 shimming (B_1^+ shim phase) to the MOS prior to shimming (equal phase) averaged over the heart; it measures the increase in transmit B_1 efficiency due to reduced destructive interferences resulting from B_1^+ shimming. The average predicted RTE over 6 subjects was 2.62 ± 0.5 meaning there was , on average, 162% more transmit B_1^+ available averaged over the heart after B_1^+ shimming for a given input power. It was shown previously that the predicted RTE derived from the B1+ shimming data is a good estimate of the measured RTE based on actual B1+ maps measured in vivo (28). Similarly, an estimate of B_1^+ nonuniformity can be determined by the standard deviation over the mean of the MOS over the ROI used for optimization in the heart. The B_1^+ nonuniformity dropped from 42% to 20% after B_1^+ shimming. The theoretical and experimental data show that improvements in B_1^+ efficiency, B_1^+ homogeneity and signal intensity can be gained by "B_1 shimming" over the cardiac ROI marked by the red oval in (Fig. 12a).

The approximation B_1^+ map is clearly inherently biased by spin density, receive B_1 profiles, spin saturation and excursions from the low tip-angle approximation. Despite these limitations our experimental results show that sheer improvements in transmit efficiency, and thus in SNR and image quality, can be obtained based on this approach. Possible reasons for this apparent robustness against multiple sources of bias may include the fact both transmit and receive magnitude B_1 profiles feature somewhat similar spatial decaying gradients as a function of the distance to the RF coils. Naturally, this does not alleviate the differences existing between receive and transmit B_1 profiles at very high field, and this latter peculiarity may reflect that the limits of the B_1^+ approximation are

most noticeable near the chest wall where the B_1^+ and B_1^- are strongest and significantly differ from each other. Recently Cunningham et al (34) proposed a rapid B_1^+ mapping technique; it is expected that a B_1^+ map will not be bound to the same limitations as the approximate B_1 map and will allow for better B_1 shimming in the heart.

The B_1^+ shimming procedure, including cable and phase shifter manipulation, took approximately 15-20 minutes per slice. Due to the time requirement of this procedure, only a single slice could be shimmed during a study. A central axial slice was found to provide the greatest global B_1^+ shim when compared to shimming on either short axis or four-chambered views. New improvements in transmitter phase and gain control will allow for slice-by-slice shimming. It is expected that slice-by-slice shimming will allow for greater B_1 efficiency, homogeneity and signal intensity as well as reductions in SAR, when compared to single slice shimming.

SAR modeling

Modeled SAR distributions are shown in Figure 13. To compare the pre- and post-shim SAR distributions, the input voltages have been adjusted so that the average flip angle over the FOV within the heart is constant between Fig 13a and 13b. For a desired B_1 transmit field over the heart, Figures 13 shows that SAR is significantly lower in the subject after B_1 shimming, as compared to the equally-phased array. The ability to reduce local SAR with phase-only based B_1^+ shimming does not extend to techniques attempting to achieve a homogeneous B_1^+ where optimization of each channel's transmit amplitude is required. In such cases, large increases in local SAR can result (35).

Regardless of the B_1^+ shimming method employed, the SAR will be proportional to the square of the flip angle with a given set of transmit phases and amplitudes.

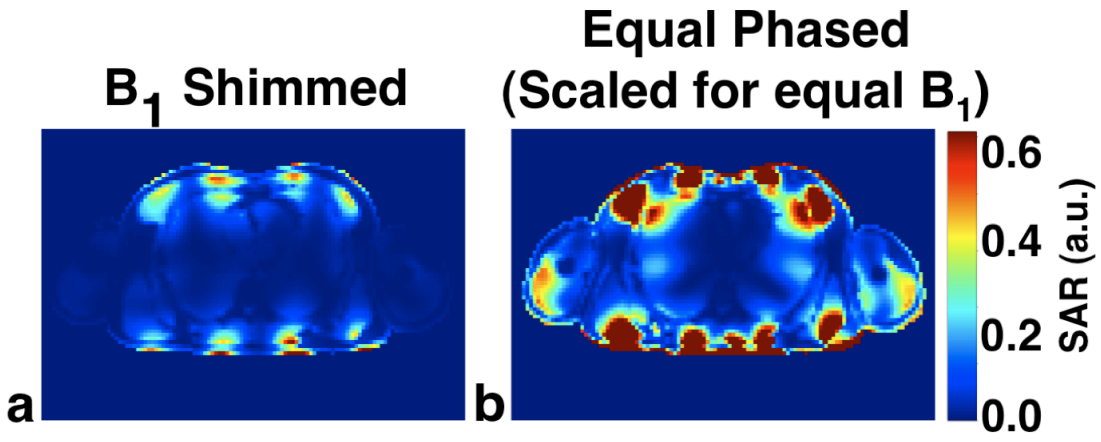

Figure 13: SAR is calculated for **(a)** B_1^+ shimmed elements, and **(b)** when all elements have equal transmit phase. The shimming method used for this simulation is described by. For a given average flip angle over the heart, a significant increase in RF transmit power and consequential SAR is required when B_1 shimming is not used

SNR Measurement

Figure 14 shows heart images resulting from different phasing of the coil elements along with associated SNR profiles. Figure 14a shows a short-axis slice in heart imaged when all eight elements equally phased (equal phase); figure 14b is the same slice, however, the anterior half of the array is set in 180° phase opposition with the posterior half (opposite phase); finally figure 14c is when the array elements are phased for maximum B_1^+ efficiency through the heart (B_1^+ shimmed). Figure 14d shows the SNR line plot for all three cases (fig 14a-c). The SNR of the blood in the right ventricle in the B_1^+ shimmed case is approximately three times greater than either the equal phased or opposite phased cases; the SNR in the septum of the B_1^+ shimmed case has improved by a factor of 2.4 over the equal phased or opposite phased cases.

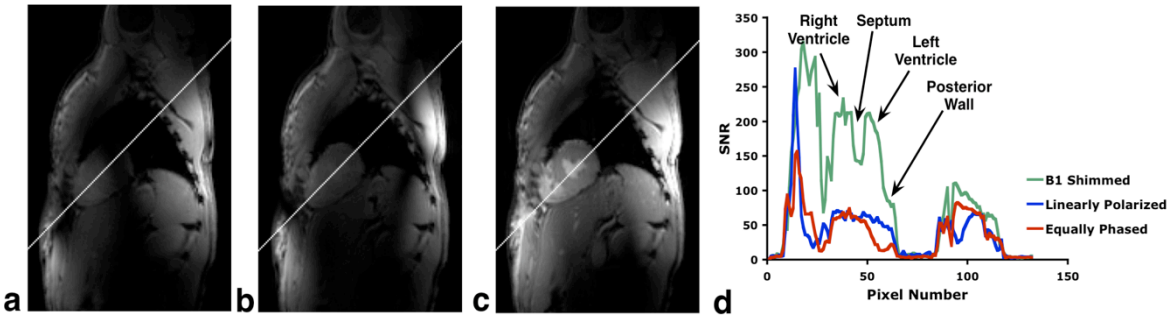

Figure 14: Gradient echo images of the heart with plots of the SNR along the indicated oblique line for **(a)** array elements equally phased, **(b)** array elements opposite phased, and **(c)** B_1^+ shimmed. **(d)** is a line plot through the chest showing the changes in SNR in the heart for the three different cases (a-c).

More importantly, the contrast between the blood and the myocardium is tremendously improved with B_1^+ shimming for a given transmit power. While the SNR is sufficiently high in all three cases, only the B_1^+ shimmed case clearly delineates the structure of the heart. Clinically, ejection fraction, myocardial mass quantification, and valvular function depend on this difference in signal intensity between blood and the myocardium; therefore, of the three images in figure 14, figure 14c has the most clinical relevance. It may be possible to achieve the same contrast in the opposite phase case, but at the cost of significantly increasing the transmit power. Therefore, for cardiac imaging, accurate phasing of the transmit channels increases the efficiency of the B_1^+ leading to both increases in SNR and contrast between the structures within the heart.

Cardiac Imaging

Figure 15 illustrates four FLASH cine images of the sixty successive phases of the cardiac cycle along the short axis and four-chamber views. These data were collected in approximately 20 seconds with isotropic in-plane resolution equal to 1.8 mm and a slice thickness of 5.5 mm. These cine frames show excellent spatial and temporal resolution

throughout the cardiac cycle. Despite the fact that B_1 shimming was performed on a single axial slice, Figure 15 demonstrates that single slice B_1^+ is sufficient to provide a reasonable global B_1 shim for the heart. The short axis images accurately show the ventricles, pericardium and pericardial fluid as well as the posterior descending artery, anterior descending artery and great cardiac vein. Strong signal and contrast are seen between the blood and the posterior wall of the heart. In the four-chamber view the atria, ventricles, mitral valve and tricuspid valve are clearly identifiable.

FLASH cines, as in Figure 15, are often used to assess cardiac function. High SNR and myocardial/blood contrast in the short and four-chambered axes would easily allow for calculation of ejection fraction, valvular function, and other clinically relevant measurements.

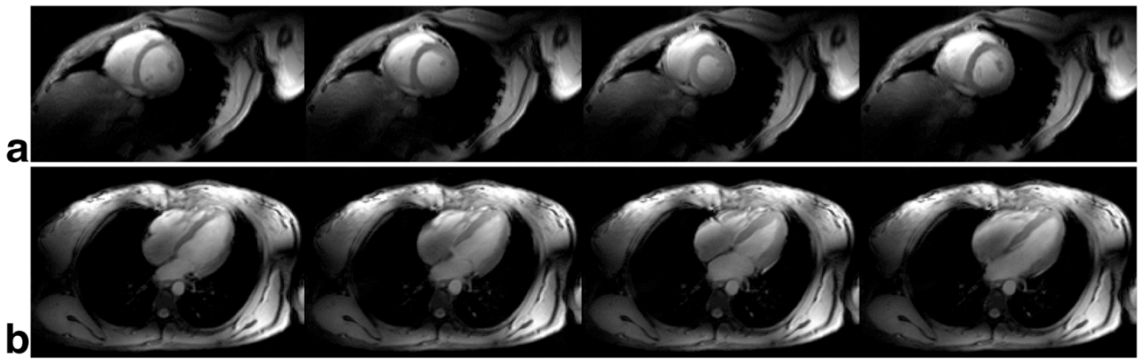

Figure 15: Four time points from FLASH cine along the **(a)** short axis and **(b)** four-chambered view. Both sets of cines were collected in one breath hold, approximately 20 sec, with spatial resolution of 1.8mm x 1.8mm x 5.5 mm.

Figure 16 shows the short axis (a) FLASH cine and (b) TSE from the same subject. The image resolution of the TSE image is 1.8 mm by 1.5 mm by 5.5 mm. Despite the lower signal at the posterior wall of the heart, these images show accurate cardiac morphology.

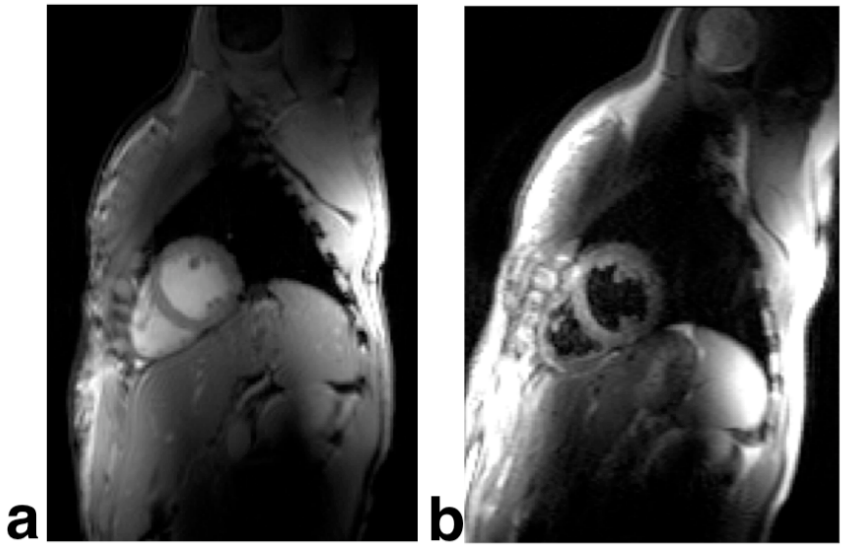

Figure 16: **(a)** FLASH cine and **(b)** TSE images of the short axis from the same subject.

TSE imaging sequences are used for measuring cardiac morphology. The high myocardial signal and nearly complete suppression of the inflowing blood in the TSE sequence facilitate imaging of anatomic features as demonstrated in the short axis image of Figure 16. TSE images are extremely sensitive to B_1^+ non-uniformities. Fig.16b demonstrates that, however, even this sequence can be used for cardiac imaging at 16 Tesla with the approach described in this paper. The degraded signal in the posterior wall of the heart in Figure 16b, is likely caused by the extreme sensitivity of the TSE sequence to B_1^+ inhomogeneities. Better B_1 shimming using arrays with larger number of elements and/or better optimization algorithms is expected and this in turn should improve the signal homogeneity and intensity along the posterior wall of the heart.

A comparison with what can be attained at other fields is not provided in this paper. Due to the significant methodological differences it is difficult, to compare these initial cardiac results at 7 T to those acquired at clinical field strengths. Different field strengths

require different imaging sequences. At 1.5 T, SSFP sequences are the standard for functional cardiac imaging, these sequences, however, work with only moderate success at 3T and are currently impractical at 7 T. Functional imaging at 7 T is currently limited to FLASH cines. Additionally, coil configurations are also different at the different field strengths. Clinical cardiac studies (both 1.5 T and 3 T) employ a volume transmit coil used in conjunction with local receiver arrays. This combination is known to improve both spatial coverage and SNR when compared to local transceive coils. A surface transceive array was used in this study because volume transmit-only 7 T body coils have not been tested. Finally, B_1^+ and B_0 inhomogeneities are significantly greater at 7 T when compared to clinical field strengths. Despite remarkable advances in B_1^+ and B_0 shimming technique, (at both 3 T and 7 T) further advances are requisite before an accurate comparison can be made. Undoubtedly, 7 T cardiac imaging will improve as hardware, protocols and methods are optimized for higher field strengths.

4.4 CONCLUSIONS

The feasibility of human cardiac MRI is demonstrated at 7 T. These early results have been achieved by solving or compensating for a number of known challenges for cardiac and ultra-high field whole body imaging related to: 1) increased MHD artifacts in the ECG waveform, 2) nonuniform RF fields due to complex destructive interference patterns, and 3) increased SAR due to increased high frequency energy losses due to the tissue permittivity and conductivity. High-resolution FLASH cines and TSE images have

been acquired with an eight-channel local transceiver array phased by a local B_1^+ phase shimming technique.

5. Comparison between eight-and sixteen-channel TEM transceive arrays for body imaging at 7 T

Originally published in *Magnetic Resonance in Medicine,* 2012, 67(4): 954-964.

Carl J. Snyder, Lance DelaBarre, Steen Moeller, Jinfeng Tian, Can Akgun, Pierre-Francois van de Moortele, Patrick J. Bolan, Kamil Ugurbil, J. Thomas Vaughan, Greg J. Metzger,

ABSTRACT

Eight- and sixteen-channel transceive stripline/TEM body arrays were compared at 7 tesla (297 MHz) both in simulation and experimentally. Despite previous demonstrations of similar arrays for use in body applications, a quantitative comparison of the two configurations has not been undertaken to date. Results were obtained on a male pelvis for assessing transmit, SNR and parallel imaging performance and to evaluate local power deposition versus transmit B_1 (B_1^+). All measurements and simulations were conducted after performing local B_1^+ phase shimming in the region of the prostate. Despite the additional challenges of decoupling immediately adjacent coils, the sixteen-channel array demonstrated improved or nearly equivalent performance to the eight-channel array based on the evaluation criteria. Experimentally, transmit performance and SNR were 22% higher for the sixteen-channel array while significantly increased reduction factors were achievable in the left-right direction for parallel imaging. Finite-difference time-domain simulations demonstrated similar results with respect to transmit and parallel imaging performance, however a higher transmit efficiency advantage of 33% was predicted. Simulations at both 3T and 7T verified the expected parallel imaging improvements with increasing field strength and showed that, for a specific B_1^+

shimming strategy employed, the sixteen-channel array exhibited lower local and global SAR for a given B_1^+.

Keywords:

7 tesla, Ultrahigh field, 7T body imaging, TEM coil, Transmit/Receive Arrays, SAR

5.1 INTRODUCTION

In the last decade, substantial improvements in MRI techniques have been achieved based on the use of ultrahigh magnetic fields (7 tesla (7T) and above) (3,27,28,36-41). To date, most ultrahigh field applications have focused on the brain where the increased field strength has benefitted anatomic, physiologic and functional investigations. These benefits were shown to arise from field dependent gains in signal to noise ratio (SNR) (42), parallel imaging performance (43,44), and contrast mechanisms that provide unique and/or improved information. Examples in the last category include, susceptibility contrast for high resolution imaging of brain function (45-48), brain morphology (49,50), and vascular architecture of the venous system (51-53). Similarly, T_1 values have been shown to disperse with increasing B_0 in the brain to provide excellent T_1 contrast for anatomic imaging (54) while increases in T_1 have lead to improved arterial angiography (55,56).

Imaging the human body at ultrahigh fields, however, poses substantial challenges. One of the main difficulties comes from the spatial inhomogeneities and reduced efficiency resulting from the constructive and destructive interferences between complex

B_1 vectors (27). At 297 MHz (proton's Larmor frequency at 7T) the RF wavelength in body tissues are comparable to or shorter than the object of interest resulting in non-uniform excitation and receive patterns due to complex RF field interferences. These interferences reduce both the RF transmit efficiency and homogeneity, potentially increasing localized power deposition as measured by the specific absorption rate (SAR) (27,57). The ability to transmit through multiple independent channels provides the most general and flexible solution to these problems using techniques like static B_1 shimming or spatially tailored RF pulses. It has been recently demonstrated that these multi-channel transmit strategies can address the complex destructive interferences and accomplish imaging even for the human torso at 7T where they pose the greatest challenge (28,39,56,58).

Due to the large size and distance from the body or low "filling factor," volume arrays at 7T struggle to generate sufficient transmit B_1 due to power limitations or SAR constraints. This has, in part, lead to surface arrays being the most common method for imaging the body at 7T. With the use of surface transceiver arrays and B_1^+ shimming strategies many different body applications have been realized including those in the prostate (28), heart (39), liver (59) and uterus (58). While most of these studies use a stripline/TEM architecture similar to that originally presented (3,60) in other types of transceiver designs have also been demonstrated in the literature (61-63).

For these surface transceiver arrays, increasing the number of coils from eight to sixteen with the same overall spatial coverage was expected to provide advantages on both transmit and receive. On transmit, increasing numbers of channels should decrease

the total power required to generate a given B_1^+ while simultaneously reducing SAR. On receive, gains in SNR would be expected along with increased parallel imaging performance. To investigate these potential gains with respect to increasing numbers of coils we compared the performance of similarly constructed eight-channel and sixteen-channel stripline/TEM transceive arrays for body imaging at 7T. These arrays were designed to be close fitting to the body to increase the filling factor, while the multiple transmit channels allowed for B_1^+ shimming and investigating parallel imaging performance. The two arrays were compared experimentally with respect to transmit efficiency, SNR, and parallel imaging performance in the male pelvis under conditions of a local B_1^+ phase shim. Additionally, simulations were performed to compare power deposition versus transmit performance at 7T and to assess the field dependent parallel imaging performance between 3T and 7T with the same arrays.

5.2 METHODS

RF coil and hardware

The eight-channel array consisted of a pair of four-channel stripline/TEM arrays, one located anterior and the other posterior to the torso (Fig. 17a). Four coils each were attached in parallel configuration to a flexible Polytetraflouroethylene (PTFE) plate measuring 227 x 356 x 3 mm thick. The individual coil structures were 153 mm long with a 12.7 mm wide inner conductor and a 50 mm wide outer conductor, separated by a 19 mm thick PTFE dielectric bar with a low loss tangent and a relative permittivity (ε_r) of 2.08. A 50 mm air gap separated each coil element. While similar in overall dimensions,

the sixteen-channel array contained eight channels on both the anterior and posterior plates. Each individual coil had the same physical geometry as the eight-channel array, with the exception that there was no air gap between coils (Fig. 17b).

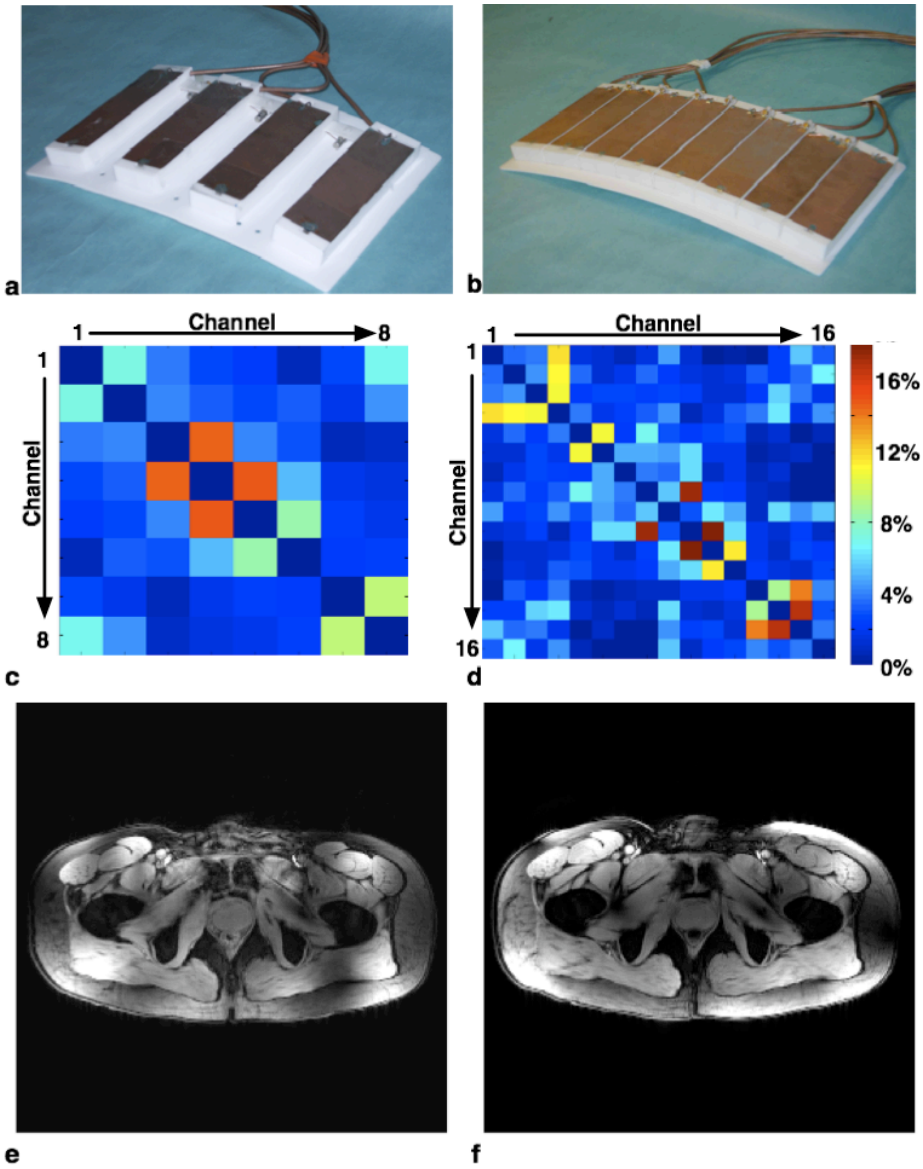

Figure 17: Anterior plate of the eight-channel (a) and sixteen-channel (b) arrays and gradient recalled echo images (c) and (d) show the spatial coverage, in the axial plane, of the eight- and sixteen-channel arrays, respectively. The corresponding covariance of the noise of the receiver chain, (e) and (f) respectively. The blue box in (e) shows the greatest coupling occurs between channels four and five in the eight-channel array while the green box in (f) shows the greatest coupling occurring between channels ten and twelve in the sixteen-channel array.

For both arrays, all coils were individually tuned to 297 MHz, and matched to a 50Ω coaxial line. Nearest neighbor coils, for both arrays, were capacitively decoupled. Fig. 18 shows the slight difference between decoupling techniques for the eight- and sixteen-channel array. In the eight-channel array, a single decoupling capacitor connecting the conductor strips was used; however in the sixteen-channel array, two decoupling capacitors were used in concert, one connecting the conductors and a second connecting the ground plates. The additional capacitive decoupling used for the sixteen-channel array was required to reach at least target isolation of 18 dB between nearest neighbor coils when loaded. All bench measurements required for coil tuning, matching and isolation were performed using a calibrated Hewlet-Packard (Palo Alto, CA) HP 4396A network analyzer together with an 85046A "S" parameter test set.

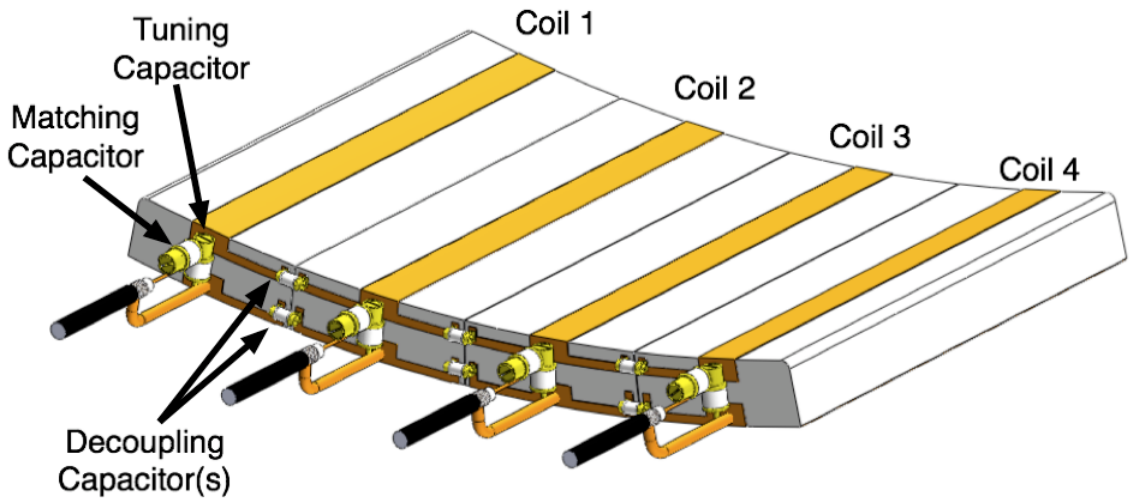

Figure 18: An example of a four-channel stripline/TEM transcieve array showing the placement of the tuning, matching, and decoupling capacitors. In the actual eight-channel array there would be a 5cm air gaps between the coils and only require the conductor strip decoupling. All tuning, matching and decoupling capacitors are 1-10 pF variable capacitors.

Great care needs to be taken when decoupling stripline/TEM arrays. While the coils in these arrays can be tightly packed, and since it is not possible to geometrically decouple these coils, like a loop array, coupling between neighboring coils can be significant. Currently there are limited methods for decoupling stripline/TEM arrays with capacitive decoupling being the most prominent. During transmit, due to the B_1^+ shim, significant current and voltage drops across the decoupling capacitors are possible, the magnitude and distribution of which can vary with B_1^+ shimming. Depending on the phase set, following B_1^+ shimming, it is possible the voltage drop across the decoupling capacitor can be nearly twice the output voltage of the amplifiers with the current through the capacitor being proportional to reactive impedance of the capacitor. This needs to be considered when determining the appropriate power rating of the decoupling capacitors. For both arrays, the decoupling capacitors had a DC working voltage of 3000 V and a DC breakdown voltage of 6000 V. For consistency, the same type of capacitors used for decoupling were used for both the tuning and matching.

Imaging experiments were performed on a 7T (ω_o=297.14 MHz) magnet (Magnex Scientific, UK) interfaced to a Siemens console and whole body gradients. Parallel transmit was accomplished by a configuration where the low power output of the console was split into eight or sixteen channels through a computer controlled phase shifter and subsequently amplified by 1 kW amplifiers, one for each channel (Communications Power Corporation, Hauppauge, NY). On receive, signal amplification was accomplished with 50Ω preamps (G = 25 dB, NF = 0.9 dB at 300MHz).

Local B_1 shimming

The theory and experimental results of local B_1^+ phase shimming were previously described (27,28). In general, the objective of B_1^+ shimming can include the optimization of transmit efficiency, the creation of a homogeneous transmit B_1, reduction of local SAR or some combination of these. In this work, we used a previously characterized B_1^+ shimming method for optimizing transmit efficiency in the region of the prostate by minimizing local B_1^+ destructive interferences (28). To account for changes in exact coil positioning and geometry, B_1^+ shimming was unique for each coil, subject, and session.

Transmit B_1 and SNR Mapping

To compare transmit and receive characteristics, both B_1^+ efficiency and SNR maps were calculated. The spatially varying flip angle was calculated using the actual flip angle imaging (AFI) method (64) (TR_1 = 20 ms, TR_2 = 120 ms, TE = 3 ms, 50° nominal excitation, 128 x 128 x 16 acquisition matrix, and a 2.7 x 2.7 x 5 mm image resolution). The transmit efficiency was calculated by converting the flip angle to micro tesla and dividing that by the square root of the net input power as measured at the coil.

The receive performance was characterized by two separate gradient echo (GRE) acquisitions. The first GRE scan was used to compare SNR throughout an axial cross-section of the pelvis. To minimize the influence of varying tissue longitudinal relaxation rates on the SNR calculations, a low resolution, fully relaxed GRE acquisition was performed (TR = 6000 ms, TE = 4.08 ms, 128 x 64 acquisition matrix, 45 degree flip angle, 3 x 6 x 8 mm image resolution, 33 kHz bandwidth and a scan time of 6 min 19 s).

While in general, the same fully relaxed acquisition would be desired to compare receive performance in the region of the prostate, it produced inconsistent results due to motion and variable susceptibility effects near the prostate-rectum interface. To address these issues, a higher-resolution GRE acquisition with a shorter TR and higher bandwidth was used to compare receive performance in the prostate region at the expense of being slightly T_1-weighted (TR= 76 ms, TE = 3.79 ms, 384 x 384 acquisition matrix, 1.3 x 1.3 x 5 mm image resolution, 10 degree flip angle, 4 averages, 100 kHz bandwidth and a scan time of 1 min 57 s). The T_1-weighting had minimal impact on the relative SNR due to accurate power calibration yielding similar flip angles with both coils in the prostate. To assist in evaluating coil coupling and for use in SNR calculations, data was also acquired without pulsing the RF amplifier to determine the noise-correlation matrix (65).

Maps of SNR are formed from the pseudo multiple replica method (66). Using the noise-correlation matrix, a series of 100 images of correlated noise are generated by forming an un-accelerated SENSE reconstruction. The image noise map is generated by calculating the standard deviation of the real value of a pixel through the series of noise images. The SNR is the magnitude of the image in the original reconstructed image, divided by the value of the noise standard deviation for that pixel. For both acquisitions, the GRE images were corrected for flip angle, referred to as normalized SNR (nSNR), to permit a comparison of SNR independent of B_1^+ variations.

Finite-Difference Time-Domain (FDTD) Simulations

Numerical Maxwell solutions of the eight- and sixteen-channel stripline transceiver arrays were calculated in an anatomically correct human body model (Duke from Virtual Family (67)) using XFDTD (Remcom Inc., State College, PA) to estimate power deposition (SAR), assess theoretical transmit, and parallel imaging performance. The body and both arrays were modeled at an isotropic resolution of 5 mm. Each coil was driven by one voltage source and tuned to proton's Larmor frequency at 7T. For a given array, all coils were simulated individually, normalized for net input power, and then optimally combined using the same B_1^+ shimming methods employed in vivo. Peak 10 gram averaged SAR in the body was determined after B_1^+ shimming. The ratio of peak local SAR (normalized to 1 W input power) divided by the square of the average $\mu T/W^{0.5}$ generated in the prostate was used as a further combined metric of coil and B_1^+ shimming performance. Theoretical parallel imaging performance was also calculated from the simulated data for comparison with 7T experimental results while the same models were run at 128 MHz to estimate geometry factors for the same array designs at 3T.

Parallel Imaging Performance

Experimental determination of parallel imaging performance for encoding spatial information was compared against simulated results for both arrays at 7T by calculating geometry factors (g-factors) under various parallel imaging conditions. Experimental calculations were performed on data acquired in vivo with a 3D-FLASH sequence (TR = 3.11 ms, TE = 1.25 ms, 20 slices, 400 x 400 x 160 mm field of view, 0.78 x

0.78 x 5.0 mm resolution and 32 s acquisition time), and simulated calculations were based on calculated B_1^- fields from the previously described FDTD simulations. Parallel imaging performance, in the form of mean and maximum g-factors, were calculated on a central slice following methods presented by Pruessmann et al (65).

Additionally, using this 3D FLASH sequence, 1-D reduction factors of 2, 4, and 8 were acquired in the left-right direction reducing the acquisition time to 16 s, 8 s and 4 s respectively. In this case, a full resolution image (R=1) acquired separately was used to calculate a 5x4 GRAPPA kernel, which in turn, was used to reconstruct the accelerated images (R>1). This meant that effectively 512 auto-calibration scan (ACS) lines were used, although far fewer would be necessary to estimate the reconstruction kernel. By performing the reconstruction in this manner, the reconstructed images are not biased by the specific GRAPPA kernel employed, thereby reflecting only the g-factor noise amplification.

5.3 RESULTS

RF coil

Table 1 shows the unloaded and loaded Q values for both arrays and the isolation between nearest-neighbor next-nearest neighbor coils for both the unloaded and loaded case. For comparison, loaded and unloaded Q values for a single element TEM coil, which is the building block for both arrays, is also reported in table 1. Both arrays show lower unloaded Q values then the single element, this attributed to the coupling to both the nearest neighbor and next-nearest neighbor coupling. The large standard deviation in

the unloaded Q's is due to the physical placement of the coils in the array; medial coils had noticeably lower Q's then the lateral coils.

	Q_U	Q_L	Q_{ratio}	S_{21U} NN	S_{21L}NN	S_{21U}NNN	S_{21L}NNN
Single Channel	143	23	6.2				
Eight-channel	125 ± 13	32±5	3.9	-15 dB	-20 dB	-12 dB	-22 dB
Sixteen-channel	127 ± 15	34±6	3.8	-21 dB	-26 dB	-11 dB	-25 dB

Table 1: The unloaded and loaded Q-values, as well as, the isolation between nearest neighbor (NN) and the next nearest neighbor (NNN) coils for both the unloaded and loaced case.

In contrast to the bench measurements, fig. 17e and 17f show the covariance of the noise for the receiver chain. In the eight-channel array, the maximum amount of coupling between any two channels was between coils 4 and 5 (15dB isolation). Similarly in the sixteen-channel array maximum coupling between any two channels occurs between coils 10 and 12 (17dB isolation).

B_1^+ Shimming

The results of local B_1^+ shimming for the sixteen-channel array are shown in Fig. 19. Prior to B_1^+ shimming, all coils were set to have an equal transmit phase (Fig. 19a); the image inhomogeneity and signal voids are due primarily to the complex destructive interference patterns of the transmit B_1 (Fig. 19c). By calculating the correct phases (Fig. 19d), the RF efficiency can be greatly increased over a specified target, in this case, the prostate (Fig. 19b). For such a small target near the center of the coil, even though not explicitly optimized, this B_1^+ shimming method greatly increases homogeneity over the same region. A theoretical discussion of local B_1^+ shimming at 7T and examples of the

B_1^+ shimming in the prostate using the eight-channel array can be found in Metzger et al. (28). Figures 17c and 17d show the axial gradient echo images acquired following B_1^+ shimming in the prostate on the eight- and sixteen-channel arrays, respectively.

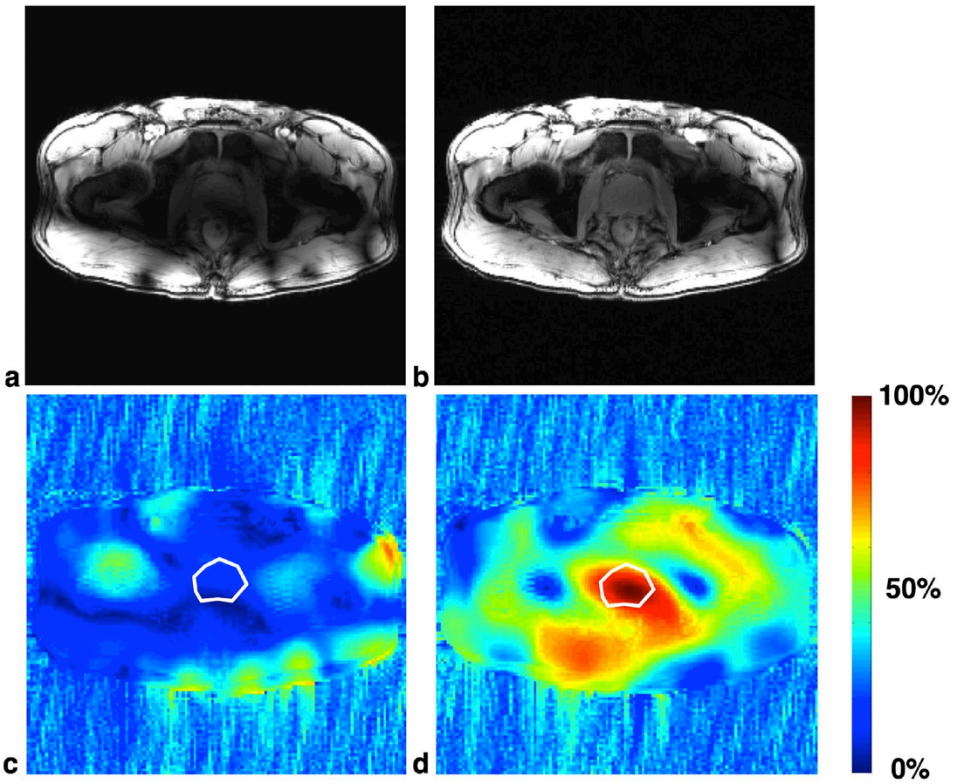

Figure 19: Representative B_1^+ shimming results in the sixteen-channel array. (a) and (b) are axial gradient recalled echo scout images before and after local B_1^+ shimming, respectively. The areas of signal dropout, or RF shading, in (a) are primarily due to complex destructive interference of the B_1^+ between transmit channels. (c) and (d) show the percent of available B_1^+ (magnitude of the sum over the sum of the magnitude of all B_1^+ fields), before and after B_1 shimming, respectively; the white polygon is the region of interest, the prostate, where the transmit efficiency was optimized. Prior to B_1^+ shimming, most of the B_1^+ from individual coils was adding destructively resulting in an available B_1^+ of 20% (c). After B_1^+ shimming, transmit efficiency is greatly increased (d).

Experimental Transmit and Receive Performance

After B_1^+ shimming in the prostate, transmit B_1 magnitude maps of the lower pelvis were calculated using the AFI method to assess transmit performance of both arrays, Fig. 20a and 20b (64). In the case shown, the transmit performance in the prostate for the

eight-channel and sixteen-channel arrays were 0.169 ± 0.017 and 0.206 ± 0.025 $\mu T/W^{0.5}$, respectively (Table 2).

		B_1^+			Local (10 g avg.)		Whole Body	
Array		Mean $\mu T/W^{0.5}$	Std Dev $\mu T/W^{0.5}$	% inhomo.	SAR/W	SAR/$(B_1^+)^2$	SAR/W	SAR/$(B_1^+)^2$
8	Sim	0.202	0.018	9%	0.355	8.70	0.008	0.188
	in vivo	0.169	0.017	10%	-	-	-	-
16	Sim	0.267	0.022	8%	0.340	4.77	0.009	0.119
	in vivo	0.206	0.025	12%	-	-	-	-

Table 2: The simulated and experimental transmit efficiency (in the prostate) along with global and local peak SAR for the both the eight- and sixteen-channel arrays. In all cases, B_1^+ shimming was used to increase the transmit efficiency in the prostate.

The nSNR images calculated from the high resolution GRE images are shown for both arrays, Fig. 20c and 20d. The nSNR in the region of the prostate was 22% higher for the sixteen-channel array compared to the eight-channel. To assess the receive performance of the two arrays across the pelvis, the fully relaxed SNR acquisition was used to generate nSNR images independent of T_1 effects. A histogram of all the voxels within the two nSNR images for the eight- and sixteen-channel arrays are shown in Fig. 21. These nSNR maps demonstrate the improved receive performance and uniformity of the sixteen-channel array especially near the periphery.

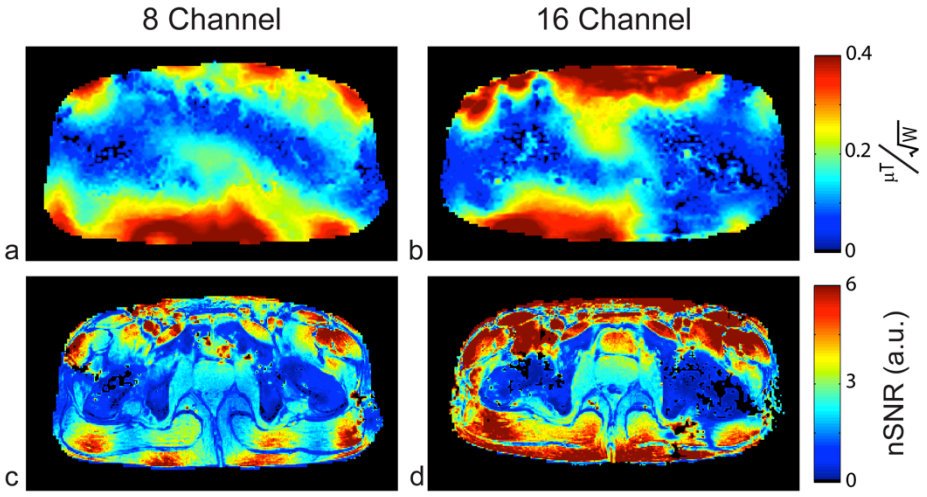

Figure 20: B_1^+ maps normalized by input power for the eight- (a) and sixteen-channel (b) arrays. SNR normalized by B_1^+ (nSNR) for the eight (c) and sixteen-channel (d) arrays generated from the high resolution GRE acquisition. The transmit performance of the sixteen-channel array is 22% higher; the nSNR in the prostate is also 22% higher with the sixteen-channel array.

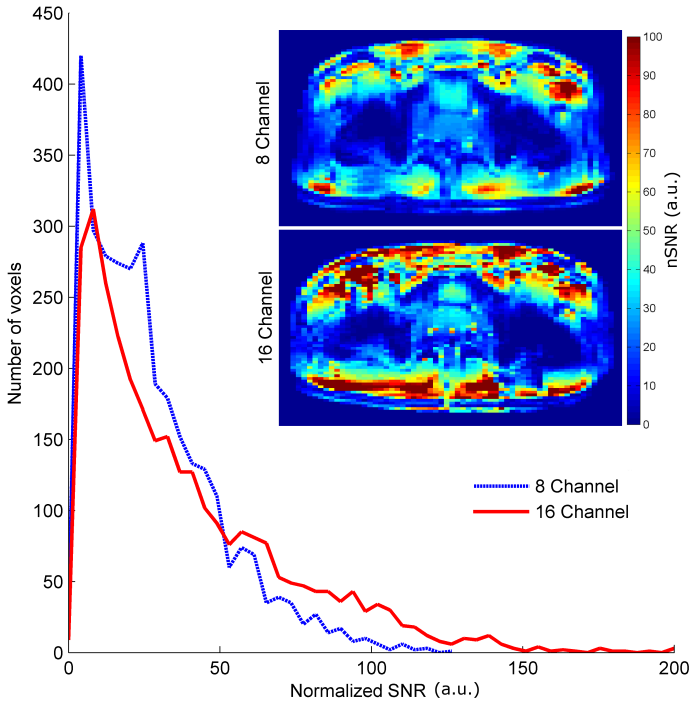

Figure 21: Histogram of all nSNR values derived from the long repetition time GRE acquisition for both the eight- and sixteen-channel arrays. Both of the nSNR images used to generate the histrogram are shown as insets. Both the images and histogram demonstrate the increased receive performance of the sixteen-channel array in the periphery. This data was acquired to better demonstrate the receive performance across the torso as it is independent of T_1 weighting.

Simulated B_1^+ and SAR

The simulated transmit performance for both arrays along with the normalized 10 gram peak local SAR and whole body SAR after B_1^+ shimming are given in table 2. Figures 22a and 22b show the position of the ROI used for B_1^+ shimming and the region over which the mean and standard deviations of B_1^+ were determined. The simulated transmit performance in the prostate for the eight-channel and sixteen-channel arrays were 0.202 ± 0.018 and 0.267 ± 0.022 $\mu T/W^{0.5}$, respectively (Table 2).

\

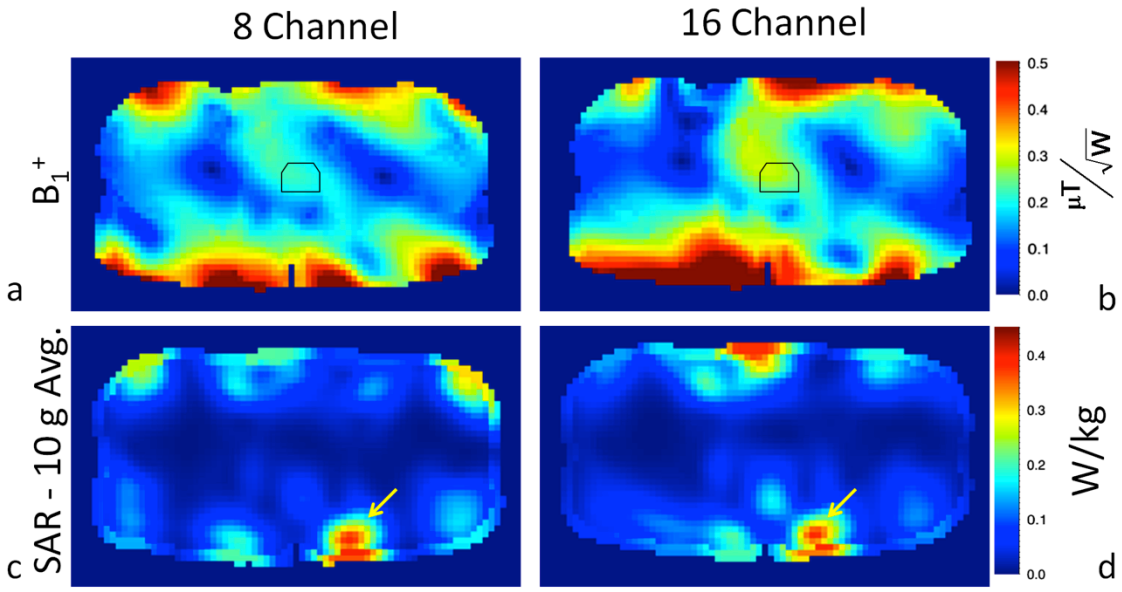

Figure 22: Simulation results for the (a) eight- and (b) sixteen-channel arrays in terms of transmit B_1 normalized by input power. 10 gram averaged SAR normalized by input power for the (c) eight- and (d) sixteen-channel arrays. The location of maximum SAR in each of the images (c-d) is indicated with a yellow arrow and the value's maximum local SAR normalized to 1 W input power are given in table 2.

Figures 22c and 22d show the 10-gram averaged SAR for the eight-channel and sixteen-channel array, respectively. The yellow arrow in figure 22c and 22d indicate the location of maximum SAR in each case. To characterize the performance of each array,

with the current B_1^+ shim solution, the ratio of the maximum local SAR per unit input power (SAR/W) to the squared average B_1^+ per watt ($\mu T^2/W$) in the target region was calculated and shown in Table 2. This ratio was $0.36/(0.20)^2 = 8.7$ and $0.34/(0.27)^2 = 4.8$ $W/kg/\mu T^2$ for the eight-channel and sixteen-channel arrays, respectively. Similar results for the whole body SAR are also reported in Table 2.

Parallel Imaging Performance

For a range of reduction factors, Table 3 shows the g-factors for the eight-channel array from the *in vivo* data, as well as modeled data for both 7T and 3T. Similarly, table 4 shows the same for the sixteen-channel array. In the tables, left-right refers to reduction factors along the x-axis and anterior-posterior refers to reduction factors along the y-axis. The "mean" represents the average g-factors from the given slices while the "max" values represent the worst case within the slice for this spatially varying parameter. Based on imaging results, a mean g-factor ≤ 1.6 produced high quality images with only nominal aliasing. Therefore, using 1.6 as the upper limit for the allowable mean g-factor, "x" by "y" reduction factors in vivo of 4 x 1 and 4 x 2 were achievable with the eight-channel array while the sixteen-channel array reached reduction factors of 8 x 1 and 6 x 2.

			7T Anterior-Posterior				3T	
	Reduction		In vivo		Model		Model	
			1	2	1	2	1	2
Left-Right	1	mean	1.00	1.02	1.00	1.01	1.00	1.00
		max	1.00	1.23	1.00	1.04	1.00	1.03
	2	mean	1.03	1.06	1.01	1.02	1.04	1.04
		max	1.25	1.30	1.07	1.08	1.14	1.15
	3	mean	1.18	1.24	1.12	1.14	1.16	1.18
		max	1.71	1.83	1.47	1.54	1.48	1.51
	4	mean	1.48	1.58	1.25	1.31	1.27	1.36
		max	2.43	2.70	2.04	2.24	1.58	2.26

Table 3: Experimental and simulated g-factors for the eight-channel array at 7T(left) and the simulated g-factors at 3T (right).

			7T Anterior-Posterior				3T	
	Reduction		In vivo		Model		Model	
			1	2	1	2	1	2
Left-Right	1	mean	1.00	1.03	1.00	1.01	1.00	1.00
		max	1.00	1.23	1.00	1.05	1.00	1.05
	2	mean	1.01	1.05	1.01	1.02	1.03	1.04
		max	1.10	1.30	1.06	1.09	1.17	1.17
	3	mean	1.03	1.09	1.05	1.07	1.14	1.15
		max	1.14	1.40	1.32	1.35	1.40	1.43
	4	mean	1.11	1.21	1.10	1.12	1.25	1.29
		max	1.36	1.65	1.35	1.39	1.71	1.81
	5	mean	1.19	1.38	1.16	1.19	1.41	1.50
		max	1.63	2.10	1.39	1.53	2.00	2.28
	6	mean	1.27	1.60	1.33	1.27	1.68	1.87
		max	1.84	2.73	1.59	2.02	2.43	3.10
	7	mean	1.38	1.98	1.31	1.41	2.16	2.55
		max	2.13	3.98	1.59	2.34	3.38	4.97
	8	mean	1.58	3.17	1.52	1.72	2.98	3.93
		max	2.78	>10	2.54	3.44	5.99	>10

Table 4: Experimental and simulated g-factors for the sixteen-channel array at 7T(left) and the simulated g-factors at 3T (right).

Tables 3 and 4 show the extremely close correspondence at 7T between simulated and measured g-factors for the eight- and sixteen-channel arrays, thus indicating that simulations can accurately model the complex B_1^- patterns present at ultrahigh field strengths. This conclusion permits us to compare 3T versus 7T performance using

simulations for a coil of the same dimensions and geometry. In these simulations, higher reduction factors with acceptable performance (mean g-factors < ~1.6 and max < ~3) were observed for the sixteen-channel array at 7T compared to 3T.

Maps of 1/g-factors from in vivo data for accelerations in the left-right direction are shown for the eight- and sixteen-channel arrays in Fig. 23 while Fig. 24 shows the GRAPPA reconstructed images from the same acquisitions. As expected, the eight-channel cannot support 1-D reduction factors greater than four, whereas the sixteen-channel array provides images with virtually undetectable image degradation for reduction factors as high as eight (Fig. 24). Even with somewhat larger image degradation, such images can still be acceptable for many applications where time resolution is critical, such as dynamic contrast enhanced studies where accurately measuring the contrast bolus can improve pharmacokinetic modeling.

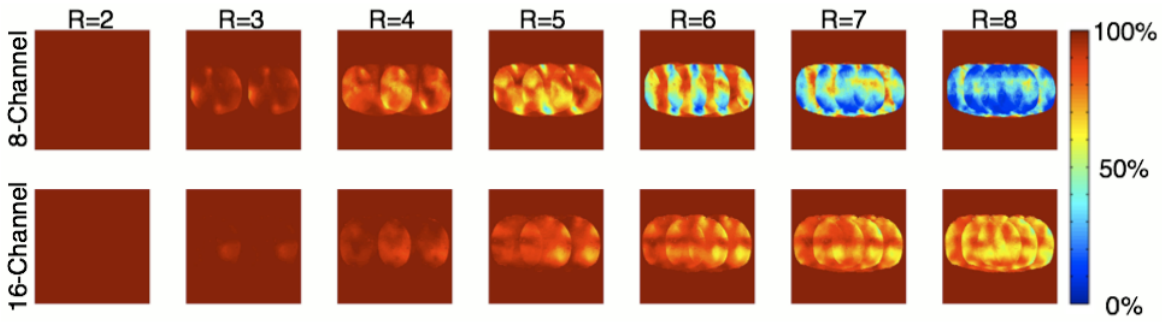

Figure 23: Experimental 1/g-factor maps in an axial slice at the level of the prostate in the human torso for the eight- and sixteen-channel arrays. One-dimensional reduction factors from 2 to 8 in the left-right direction are shown. The sixteen-channel array displays substantial improvements in g-factors over the eight-channel. For example, at a reduction factor of 4, the eight-channel array has a mean reduction factor of 1.48 with a maximum g-factor of 2.43 while the sixteen-channel has a mean g-factor of 1.11 and a maximum g-factor of 1.36.

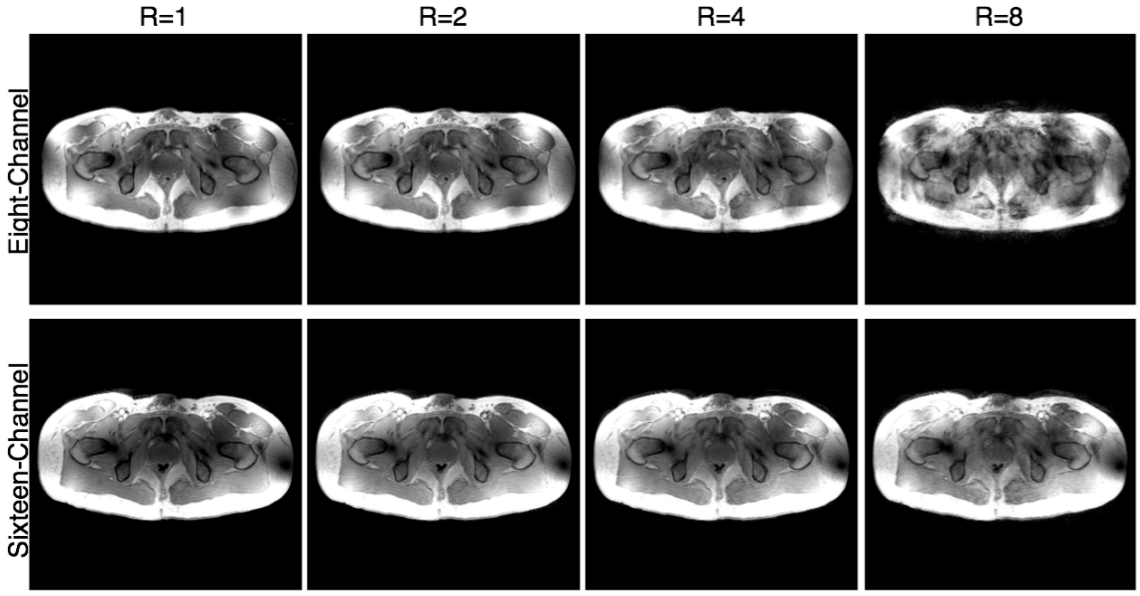

Figure 24: From left to right, GRAPPA reconstructed 3D FLASH images of the full dataset (R=1) and at reduction factors of two (R=2), four (R=4) and eight (R=8) are shown for both coils. All reductions are 1-D in the left-right direction. The acquisition time for the full field of view image was 32 s and only 4 s for the eight-fold reduction.

5.4 DISCUSSION

Although preliminary studies have shown the feasibility of imaging the torso at 7T, further RF coil and array design developments can improve performance. At lower field strengths, a large single-channel body coil is often used for excitation and combined with local receive-only surface coils. Vaughan et al (41) have previously shown that the single channel volume coil is impractical at 7T because the reduced wavelengths in the human body at 300 MHz create substantial destructive interferences resulting in RF shading (27). While this phenomenon can be seen at lower field strengths, adjusting the phase and current on the individual current carrying rungs of the body coil once can create a "universal" RF shim adequate for most patients (2). This is not the case at 7T

where body imaging requires the use of multiple transmit arrays that allow subject-dependent and region-specific optimization of B_1^+.

RF Array

In this paper, an eight- and a sixteen-channel TEM/Stripline array were compared with respect to transmit and receive performance through in vivo imaging and simulation. A TEM array design was chosen because of the compact physical size and the known efficiency of TEM arrays at high fields (2,3). The two arrays were compared on transmit, receive, SAR and parallel imaging performance.

Both arrays were designed and constructed to be nearly identical, where the physical dimensions of the individual coils as well as the overall size of the arrays were nearly identical. Both arrays were constructed out of identical materials and built, tuned and matched in the same manner. The main difference between the two arrays is the method of decoupling. When loaded, the eight-channel array was able to achieve greater then 18dB isolation between nearest neighbor coils by using capacitive decoupling on the conductors alone. A similar level of isolation was not achievable on the sixteen-channel array without the addition of decoupling capacitors on the ground plates. While ground plate decoupling capacitors could have been added to the eight-channel array, it was considered unnecessary. Decoupling capacitors are lossy, can create parasitic current loops, field perturbing loops, and potentially destroy the desired field profile of the coil, therefore the least amount of decoupling possible to achieve greater than 18dB of isolation between nearest neighboring channels was used.

Individual coil geometries were optimized, based on previous 7T transcieve coils and arrays, to maximize penetration while minimizing crosstalk. Kumar and Bottomley found the center conductor's width to only weakly determine the intrinsic single to noise ratio of a stripline/TEM or planer strip coil, with the optimal conductor strip width equal to dielectric width. We chose a slightly smaller width to dielectric height ratio to reduce the coupling between neighboring coils.

Transmit B_1 Performance

The experimentally measured B_1^+ performance and transmit efficiency advantage of the sixteen-channel array were lower than those predicted by simulation despite performing in vivo studies on a subject with similar body characteristics and dimensions as the body model. While achieving exact correspondence between simulation and in vivo measurements would be desirable, there are several factors which can account for the majority of the observed differences in our study. First, while we do include component losses for the capacitors and conductors in the simulation, the coil efficiency is still overestimated when compared to the physical coil. Because of the high density of coils and additional decoupling required, the overestimation is greater for the sixteen-channel array thus reducing the transmit efficiency gains predicted by simulation. Second, the power used to normalize the B_1^+ when characterizing transmit efficiency is obtained in simulation from the net input power, all of which reaches the coil. Experimentally however, we use the incident power to normalize the measured B_1^+ where in reality some is reflected. Reflected power can vary depending on the coil specific

matching and on the specific B_1^+ shim applied. Underestimating the coil losses and overestimating the power that enters the coil experimentally results in a lower transmit efficiency however, it also yields a conservative estimate of local and global SAR.

Impact of Coil Number on SAR and B_1^+ Optimization

In the work by Lattanzi et al. (68), the principle of ultimate intrinsic SAR (the lowest possible SAR independent of coil design) was used to compare optimization strategies using various SAR and transmit B_1^+ constraints. With the combined goal of obtaining a uniform B_1^+ with global SAR reduction, Lattanzi demonstrated that global SAR approaches the ultimate intrinsic SAR as the number of transmit channels increase. Even though in the current study we optimized our transmit B_1^+ to minimize destructive interferences with a much simpler phase based approach, a reduction in global (36%) as well as local (45%) SAR was observed with the sixteen-channel array after normalizing by B_1^+ (Table 2).

Many factors affect SAR and B_1^+ performance beyond the specific configuration of an array including the size, location, and optimization goal of the B_1^+ shimming strategy as well as the size, shape, and composition of a given subject. Beyond the simple B_1^+ shimming strategy employed in this study, the phases and amplitudes could be optimized to generate a nearly equivalent B_1^+ and similar homogeneity with substantial decreases in maximum local SAR. For example, Van den Bergen et al. (69) demonstrated through simulation that B_1 shimming can be performed while explicitly optimizing for SAR reduction to great effect at 7T when using a twelve-channel TEM volume array. Future

studies are warranted to investigate the impact of arrays with varying numbers of coils on such optimization strategies.

Along with local SAR, the available power also greatly limits which B_1^+ shimming strategies can be practically employed. If a SAR reduction or homogeneity solution were used, power efficiency can drop dramatically (69). For body applications, even when using the power efficient phase-only approach employed in this work on a small region of interest, it is difficult to generate the peak B_1^+ desired for certain applications. Therefore, employing less efficient strategies become increasingly challenging. This problem is exacerbated by the limited total power available on most multi-transmit channel 7 tesla systems. On most multi-transmit channel 7 tesla systems, each channel is driven by a 1 kW amplifier. Even modest increases in transmit efficiency, as observed experimentally in this study with the sixteen-channel array, can benefit applications which require high peak B_1^+ such as spectroscopy and inversion prepared imaging sequences.

Parallel Imaging Performance

Parallel imaging performance is expected to improve as the relative object size (object dimensions versus the wavelength) increases (44). The results presented in this paper were first shown by Snyder et al (60) and closely follow Wiesinger's (44) theoretical results that large reduction factors can be obtained in the human pelvis at higher field strengths with a moderate number of receiver coils. There is clearly a large gain achieved with sixteen-channels compared to eight-channels at 7T. With the sixteen-

channel array an 8x1 reduction can be attained with excellent average and maximum g-factors.

Tables 3 and 4 show substantial agreement between our experimental data at 7T and the g-factors predicted by simulation. This provides confidence that modeling can be used to predict the g-factors for these arrays at other field strengths. Tables 3 and 4 also show the predicted g-factors for identical eight- and sixteen-channel arrays at 3T. There is little difference in parallel imaging performance between 3T and 7T for the eight-channel array. This is likely because the coils are placed sufficiently far apart in the eight-channel design to yield spatially distinct sensitivity profiles at both field strengths. However, with the sixteen-channel array, further significant gains in parallel imaging performance are achieved at 7T which are not realized at 3T. This would be expected based on the relative object size (43,44).

The improved parallel imaging performance for the sixteen-channel array is primarily in the left-right direction, which is optimal for many imaging studies of the torso. For an axial orientation, some applications in the torso take advantage of a reduced field of view in the anterior-posterior (AP) direction when phase encoding in that same direction. Performing the phase encoding in this manner allows the spatial resolution to be maintained while reducing the scan time as fewer phase encode lines are required. However, phase encoding in the AP direction is susceptible to motion artifacts from respiration, bowel and other sources. This is especially true for the arrays described in this work because of the high intensity and inhomogeneity of the transmit and receive B_1 fields immediately adjacent to the coil. In the case of prostate imaging, most axial data

sets are acquired with a left-right phase encode to minimize artifacts in the region of interest resulting from the abdominal wall (or the endorectal coil if present). Dynamic contrast enhanced MRI is a typical example, which typically uses parallel imaging acceleration in the left-right direction to increase the temporal resolution for resolving the arterial input function and the tissue time courses. For non-contrast enhanced renal angiography at 7T, the phase encode direction is also in the left-right direction to avoid artifacts from bowel motion (70).

Finally, while not experimentally demonstrated in this work, these RF coil arrays can be used to generate spatially targeted and accelerated RF pulses using parallel transmit methods. For the same reasons the sixteen-channel array outperforms the eight-channel array in parallel imaging on the receive side, it would be expected to lead to higher "accelerations" in transmission as well.

5.5 CONCLUSION

Eight- and sixteen -channel stripline/TEM surface arrays were compared for body imaging at 7T both through simulation and experimentation. For this comparison local phase based B_1^+ shimming was employed to minimize the destructive interferences in a region surrounding the prostate as a basis for comparing transmit, receive and parallel imaging performance as well as local and global SAR. Experimentally, the sixteen-channel array demonstrated a 22% increase in transmit and receive performance in the target anatomy of the prostate. Advantages in receive performance increased for the sixteen-channel array when moving from the center of the body towards the periphery

(closer to the coil elements). While the gain in transmit and receive performance are significant for the sixteen-channel array, the most substantial advantages are arguably the greatly improved parallel imaging performance and the potential for reducing local and global SAR.

The issues that arise from positioning the stripline/TEM coils immediately adjacent to each other in the sixteen-channel array have to be considered along with the realized and potential advantages. In contrast, the increased coil spacing in the eight-channel array reduces coupling between channels and decreases complexity in construction and optimization. Determining which coil to use at a given site and for a particular application will depend on several factors including the RF amplifier configuration, requirements on peak B_1^+ and homogeneity and the availability of B_1^+ optimization methods and parallel transmit capabilities.

6. Automating the tuning and matching process of a sixteen-channel transmit-only TEM array with a thirty-two-channel receive-only loop array for body imaging applications at 7T

To be submitted to Magnetic Resonance in Medicine, Autumn or Winter 2013

Abstract

A sixteen-channel transmit-only TEM surface array to be used in combination with a thirty-two channel receive-only loop surface array was designed for body imaging application at 7T. Additionally, an electromechanical method using piezoelectric actuators and a feedback control loop was designed to automate the tuning and matching procedure for the transmit-only array. The feedback loop consisted of a dual directional coupler and reflectometer, microcontroller and signal generator. The dual directional coupler and reflectometer were placed at the coil head and measured the reflection coefficient. The microcontroller, using the reflection coefficient information, used a turn-based gradient descent empirical algorithm to automate the tuning and matching process. The signal generator supplied a 2ms square pulse, with a 10% duty cycle at 30dBm power. Additional components of the feedback control loop included multiplexors and optical switches, low pass filters and piezo controllers. As a result, each coil within the transmit array could be tuned to resonance with at least -23dB match in approximately 50-70 seconds. It is believed these advancements, specifically the automated tuning and matching process is one of the steps that will help move 7 tesla scanners to a more clinically relevant system.

6.1 Introduction

Over the past seven years, substantial improvements in MRI techniques have been achieved at ultrahigh magnetic field strengths (7 tesla (7T) and above). While most ultrahigh field applications were first focused on the brain where the increased field strength has benefitted anatomic, physiologic and functional investigations now significant improvements have occurred in body applications. These benefits, in both the head and body were shown to arise from field dependent gains in signal to noise ratio (SNR), parallel imaging performance , and contrast mechanisms that provide unique and/or improved information.

Imaging the human body at ultrahigh fields, however, poses substantial challenges. One of the main difficulties comes from the spatial inhomogeneities and reduced efficiency resulting from the constructive and destructive interferences between complex B_1 vectors (27). At 297 MHz (proton's Larmor frequency at 7T) the RF wavelength in body tissues are comparable to or shorter than the object of interest resulting in non-uniform excitation and receive patterns due to complex RF field interferences. These interferences reduce both the RF transmit efficiency and homogeneity, potentially increasing localized power deposition as measured by the specific absorption rate (SAR) (27,57). The ability to transmit through multiple independent channels provides the most general and flexible solution to these problems using techniques like static B_1 shimming or spatially tailored RF pulses. It has been recently demonstrated that these multi-channel transmit strategies can address the complex destructive interferences and accomplish

imaging even for the human torso at 7T where they pose the greatest challenge (28,39,56,58).

Due to the large size and distance from the body or low "filling factor," volume arrays at 7T struggle to generate sufficient transmit B_1 due to power limitations or SAR constraints. This has, in part, lead to surface arrays being the most common method for imaging the body at 7T. With the use of surface transceiver arrays and B_1^+ shimming strategies many different body applications have been realized including those in the prostate (28), heart (39), liver (59) and uterus (58). While most of these studies use a stripline/TEM architecture similar to that originally presented (3,60) in other types of transceiver designs have also been demonstrated in the literature (61-63).

To date, most body imaging applications at 7T have used transceiver arrays, using the same coils for transmit as receive. While most commercially available systems have thirty-two or more receiver channels, the use of a transceiver limits the number of receiver elements, in essence the number of transmit channels, usually sixteen-channels or less. The implication of this is limited SNR, lower parallel imaging performance, as well as, possible increases in SAR due to the proximity of the array to body during transmit. To investigate the potential benefits of separating the transmit array from the receiver array, at sixteen-channel TEM transmit only array was constructed to be used in concert with a thirty-two channel loop receive-only array.

Additionally one of the problems with using a surface transmit array is the required tuning and matching each transmit element at the beginning of each scan. Having a mistuned or matched transmit array can lead to reduced B_1^+ efficiency, reduced B_1^+

shimming capabilities, reduced parallel transmit capabilities, possible increases in SAR and tissue heating, possible increases coil coupling and if the array is a transceiver losses in SNR. The problem with manually tuning and matching each coil in the array is that it is time consuming and tedious and prone to user error. Of course these problems increase and propagate as the number of channels in the array increases. Automating the tuning and matching process would address and possibly alleviate these problems. To investigate the possibility of automating the tuning and matching process, an electromechanical solution was developed. Here, piezoelectric actuators were fastened to sliding cylindrical tuning and matching capacitors. Piezoelectric motors are one of the few motors that can work in strong magnetic fields; the actuators were used to manipulate and change the surface area between the center and outer plate of the cylindrical capacitors, thus changing the capacitance. This was paired with a feedback loop that monitored the reflection coefficient of the coil being tuned. The efficiency and effectiveness of this method was investigated.

6.2 METHOD

RF Array

The RF array design, shown in figure 25, consisted of a pair of arrays, an anterior and posterior array. Both the anterior and posterior array consists of two separate and distinct arrays: a eight-channel TEM transmit-only array and a sixteen-channel loop receive-only array (fig 25a). Figure 25b shows how the two arrays are placed on the body.

The sixteen-channel TEM transmit-only array was based on previous designs (4). The individual sixteen TEM coils in the transmit array were 153 mm long with a 19.1 mm wide inner conductor and a 50 mm wide outer conductor, separated by a 19 mm thick PTFE dielectric bar with a low loss tangent and a relative permittivity (ε_r) of 2.08. All sixteen coils were fastened to two rigid 6.4 mm thick G-10 fiberglass epoxy laminate ribs and housed in cast urethane polymer housing. The array housing has a width of 397.5mm a length of 161.9mm and has a curvature of a radius of 490.1mm.

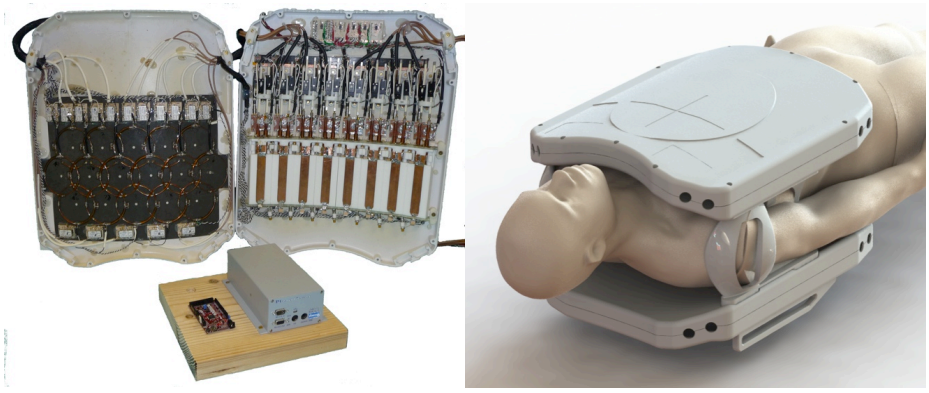

Figure 25: (a) One-half of the array with the case open to show the transmit array, receiver array and automated tuning and matching hardware; (b) placement of the array on the human body.

The tuning and matching capacitors were composed of sliding cylindrical capacitors. The outer plate of the cylindrical capacitor consisted of a copper cylinder 10mm in diameter and 30 mm in length. The center plate of the cylindrical capacitor was a copper cylinder 8mm in diameter and approximately 40mm in length. The two plates were separated by a 1mm thick PTFE dielectric. This capacitor allows for approximately 0-12pF of capacitance.

Nearest neighbor coils, were capacitively decoupled using two decoupling capacitors in concert, one connecting the center conductors and a second connecting the ground

conductors, as described previous (4). This decoupling method was required to reach at least a target isolation of 18 dB between nearest neighbor coils when loaded.

The thirty-two loop receive-only array was also based off of a previous design (71). Similar to the transmit array the receiver array is composed of two identical sixteen-channel arrays. Each sixteen-channel array is comprised of three rows of coils, the first and third row both contain five coils while the middle, or second row contains six coils. The overall length and width of the array sets are 33 and 43 cm respectively. Both sixteen-channel arrays were fixed to the interior.

Each individual coil is comprised of Number 10 AWG copper wire formed to a 9 cm circle, soldered to a RT/duroid 5880 high frequency laminate (Rogers Corp, Chandler, AZ) and tuned to proton's Larmor frequency at 7T (296.8mHz). Nearest neighbor coils had 2 cm overlap. Low impedance preamps (G=20dB, NF= 0.5dB at 300MHz; Microwave Technologies, Fremont, CA) were used for preamplifier decoupling. Both active and passive detuning was used to insure isolation between the transmit array and receiver array during transmit.

All bench measurements required for coil tuning, matching and isolation were performed using a calibrated Hewlet-Packard (Palo Alto, CA) HP 4396A network analyzer together with an 85046A "S" parameter test set.

Automated Tuning and Matching Hardware

Automating the tuning and matching process of the transmit array, requires an elaborate feedback loop, this loop for a single coil is shown in figure 26.

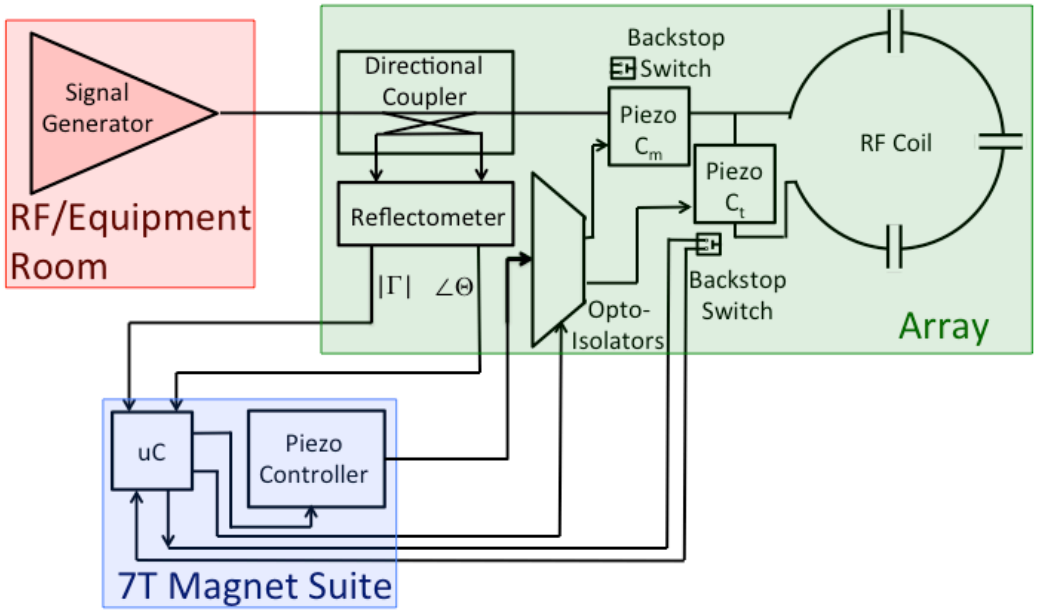

Figure 26: Diagram of the complete feedback control loop of the automated tuning and matching process fro a single coil. Also showing the respective location of each component in the feedback loop.

Piezo C_m, C_t and RF coil

The RF coil in figure 26, is a TEM transmit-only coil described above. Piezo C_m and piez C_t are the cylindrical capacitor assemblies, physically connected to a piezoelectric actuator. The piezoelectric actuator is Nexact 310 (Physik Instrumente, Germany) with 5N of push/pull force and 125mm walk range. The actuator is mechanically fastened to the center plate of the cylindrical capacitor via threaded brass machine bolt and a nylon spacer.

Piezo Controller

The piezo controller is a waveform generator that produces the waveforms necessary to drive the actuators forward and backwards. The piezo-controller is the E-861 (Physik Instrumente, Germany) linear drive controller specifically designed for the Nexact 310 actuator.

Opto-Isolators

In figure 26 only one piezocontroller is used to drive all the piezoelectric actuators. To accurately drive the actuators, the four drive waveforms from the controller need to be multiplexed between the actuatiors. The opto-isolators used to create the multiplexor, were Panasonic's AQV-252 HE1 Photo MOS's (Panasonic, Japan).

Reflectometer

The reflectometer samples the coupled incident and reflected power and outputs the phase and magnitude of the reflection coefficient of the device under test, in this case, the coil. In essence, the reflectometer serves as a low-cost network analyzer positioned near the directional coupler at the coil head. The reflection coefficient information is then sent to the microprocessor, where it is sampled and digitized.

At the heart of the designed reflectometer is Analog Device's AD8302 RF/IF gain and phase detector integrated circuit (Analog Devices, Norwood MA). The AD8302 consists of a pair of closely matched demodulating logarithmic amplifiers; each amplifier having a 60dB measurement range.

Directional Coupler

The directional coupler is a four-port passive asymmetric power divider. This is a narrow-band, lumped-element, bi-directional coupler composed of two high-pass pi networks and two coupling capacitors. It was chosen because of its compact footprint, easy implementation, high directivity and isolation as well as its low insertion loss.

The directional coupler and reflectometer were combined on board (fig 27a) and placed at the transmit coil head to reduce errors standing waves. Figure 27a also shows a resistor pi network on the coupled incident signal line. This pi network provides an addition 20 dB of attenuation to the incident signal. The reason for this is that the reflection coefficient measurement of AD8302 reflectometer is most accurate when the magnitude input signal levels are equivalent. Therefore, the reflectometer will be most accurate when the reflected signal is approximately 20 dB less then the incident signal.

Crossed pair diodes were also added to both coupled lines to protect the reflectometer during imaging experiments.

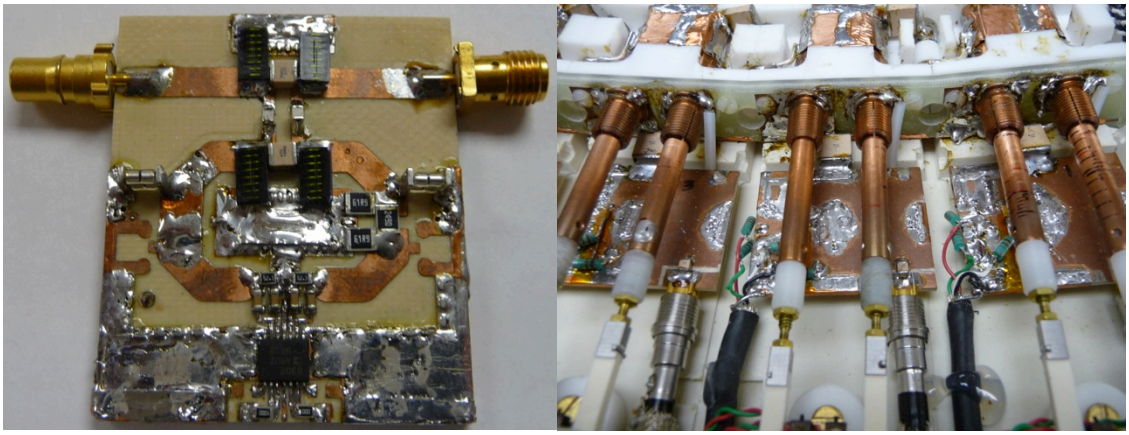

Figure 27: (a) The combined directional coupler and reflectometer board; (b) the placement of the combined board in the array

Microcontroller

The microcontroller in figure 26 is chipKit's Max32 microprocessing development board. The Max32 board uses the PIC32MX795F512 microcontroller. This microcontroller features a 32-bit MIPS processor core running at 80Mhz, 512K of flash program memory, 128K of SRAM data memory and 83 digital I/O pins of which 16 are analog inputs. Additionally, the processor provides a USB 2 OTG controller, 10/100

Ethernet MAC and dual CAN controllers that can be accessed via add-on I/O shields. The Max32 can be programmed using an environment based on the original Arduino IDE modified to support PIC32. In addition, the Max32 is fully compatible with the advanced Microchip MPLAB IDE and the PICKit3 in-system programmer/debugger.

Backstop Microswitch Detectors

The backstop switches are used to determine when each capacitor is at the home position (~0.5pF). The backstop switches are normally open (NO) non-magnetic micoswitch detectors. The specific switch used here were Panasonic's ECE2121AT (Panasonic, Osaka, Japan). Each piezoelectric capacitor was fitted with a microswitch, placed on the actuators assembly. Additionally, a small nylon beam is cantilevered off of the actuating rod of the piezoelectric actuator, pointing towards the backstop switch detector. A 3.3V signal is outputted to the backstop switch detector, when the piezoelectric capacitor is in the home position, the cantilevered nylon beam depresses the NO backstop switch detector and closes the circuit and the 3.3V signal returns back to the chipKit Max32 prototyping board.

Signal Generator

The signal generator is a 1KW RFPA (Stolberg, Germany); this is the standard Siemen's amplifier for parallel transmit systems. During the tuning and matching process an individual amplifier would pulse a 2ms square ("hard") pulse with 30dBm peak power with a 10% duty cycle.

Lab experiments were performed using a calibrated Hewlet-Packard (Palo Alto, CA) HP 4396A network analyzer together with an 85046A "S" parameter test set. The bandwidth of the network analyzer was set to 1Hz (the Larmor frequency) CW with peak power of 20dBm.

Multiplexors

To reduce the number of control and signal lines between the array, microcontroller and piezo controller, a five additional multiplexors were used. The first multiplexor was configured as a demultiplexor used to reduce the number of control lines to opto-isolators from the microcontroller. The second and third multiplexors are also 1 to 16 mux used for the backstop switches; one of the multiplexor is used to demultiplex the signal to the correct backstop switch while the other is used to multiplex the signal back to the microcontroller. The digital logic, or selector inputs for these two multiplexors is the same for the first multiplexor to the opto-isolators. The fourth multiplexor is actually two 8 to 1 multiplexors. It is used to multiplex the correct reflection coefficient information to the microcontroller. To the right of this multiplexor is a low-pass filter bank; this is used to remove any RF on the DC reflection coefficient signal lines. The fifth multiplexor supplies DC power the correct reflectometer. This is the only source where multiplexing is not used to reduce control lines, it is used to reduce possible errors in the reflection coefficient information.

Algorithm Driving the Automated Tuning and Matching Process

A turn-based gradient decent empirical algorithm was developed to automate the tuning and matching process. The empirical algorithm works as follows. To start, both the tuning and matching capacitor are brought back to the home position such that both capacitors are approximately 0.5pF. Then starting with tuning capacitor, the tuning stub is divided into six equally spaced positions (the tuning stub is approximately 30mm long, therefore each position is approximately 5mm apart). Using the actuator to move the tuning stub, the reflection coefficient is measured at each position. The position with the smallest reflection coefficient is recorded and the using the actuator, the tuning stub is moved to position just prior to the position with the smallest reflection coefficient. Once the "tuning" tuning stub is positioned, the same process is repeated with the "matching" tuning stub.

The reason why both the "tuning" and "matching" tuning stubs were placed at the position just prior to the position with the smallest reflection coefficient is because it significantly reduces the search space. The optimal capacitance and subsequently, search space, is now between the position just prior and just post the position with the smallest reflection coefficient. This reduces the search space to approximately 1/3 the original search space.

A second iteration of searching starts again. Starting with "tuning" tuning stub, the search space is divided into six equally spaced positions (the search space is approximately 10mm, so each position is approximately 2mm apart). Again the reflection coefficient is measured at each position and the tuning stub is repositioned to

the position just prior to position with the smallest reflection coefficient. This is repeated with the "matching" tuning stub.

If the coil has not fulfilled the tune and match requirements, a third round of tuning and matching can be performed. This time each position is less then 1mm apart.

6.3 RESULTS AND DISCUSSION

RF array

The Q, coupling and efficiency of the both the TEM transmit-only and loop receive-only array were recored; as expected, the values of these arrays closely match the values of previously reported arrays of very similar design.

Automated Tuning and Matching Process

Directional Coupler

The directional coupler is a narrow-band, lumped-element, bi-directional coupler composed of two high-pass pi networks and two coupling capacitors. It was chosen because of its compact footprint, easy implementation, high directivity and isolation as well as its low insertion loss. In his specific design the two pi-networks create a 90° phase shift at 297MHz, while the coupling capacitors where chosen to provide the right coupling factor. The modeled coupler is well matched to a 50 Ω line (S_{11}=-38dB) and there is high isolation between ports one and three (S_{31} = -80dB) while maintaining the correct coupling (S_{41}=-35dB), insuring high directionality of the coupler. The scattering parameters for the actual coupler are in agreement with the modeled coupler. The scattering parameters for the built coupler are S_{11}=-25dB, S_{31} = -69dB, S_{41}=-34.5dB. The

match is a little lower on the actual coupler, however, still less then 1% of the forward signal is being reflection. Additionally, the isolation between ports one and three is smaller then that of the modeled coupler, however, it is believed that this is due to the noise floor of the network analyzer and not the coupler implantation itself.

Reflectometer

A reflectometer is a device that samples or monitors the coupled incident and reflected power and outputs the phase and magnitude of the reflection coefficient of the device under test, in this case, the coil. In essence, the reflectometer serves as a low-cost network analyzer positioned near the directional coupler at the coil head.

The measurement accuracy of this reflectometer is significantly affected by board level details. For example, the minimum detectable reflection coefficient is set by the finite directivity of the coupler,$|\Gamma_{min}(dB)| < |D(dB)|$. Additionally, minor changes in line lengths between the coupled incident and reflected power and input of will create phase sensitive errors. For this reason, the reflectometer and directional coupler were placed on one board (figure 27). The overall dimensions of this board is (50mm x 50mm) and designed to be placed at the coil head (figure 27b); the board was placed "upside down," or with the ground plate "facing" the coil, this was done to help shield both the coupler and reflectometer from any parasitic radiated field from the coil.

Figure 27a also shows a resistor pi network on the coupled incident signal line. This pi network provides an addition 20 dB of attenuation to the incident signal. The reason for this is that the reflection coefficient measurement of AD8302 reflectometer is most accurate when the magnitude input signal levels are equivalent. Therefore, the

reflectometer will be most accurate when the reflected signal is approximately 20 dB less then the incident signal.

The measured DC voltage magnitude and phase were calibrated against the measured reflection coefficient of a TEM coil. These measurements were performed using a calibrated Hewlett-Packard (Palo Alto, CA) HP 4396A network analyzer together with an HP 85046A "S" parameter test set. The data was collected at single frequency, 297MHz. The DC voltage output of the reflectometer was sampled using a chipKit Max32 (Digilent, Pullman, WA) prototyping board. For every measurement, the Max32 micorprocessing board sampled the output voltage of the relfectometer 50 times over 50 microseconds, the average and standard deviation of the reflection coefficient was then calculated.

There is significant linearity between measured reflection coefficient from the network analyzer and calculated value from the reflectometer. The reflectometer's error in the magnitude of the reflection coefficient increases as the reflection coefficient increase, which is expected. However, most of this error occurs when the magnitude of the reflection coefficient is greater then 0.7; this is of little concern, as it is known that the coil is significantly mistuned. The parabolic curve of the phase information is also expected as the AD8302 can only determine phase between 0 and ±180° and is in agreement with AD8302's datasheet. It is known that if two AD8302 are configured in a reflectometer mode and used in concert, the entire phase range can be determe (i.e. 0-360°). This however, is unnecessary for this application since the coil tuning will start

from a “home” position, with a known phase. From here the phase can be continuously monitored and updated.

Automated Tuning and Matching Algorithm

The turn-based 2D root finding algorithm was the second algorithm tested. The first algorithm tested used an analytical solution. Starting from the home position it converted the reflection coefficient of the loaded coil to the complex impedance and adjusted the tuning and matching capacitors until the coil was resonant and matched to 50Ω.

In short, starting with the matching capacitor, the capacitance would be increased until the complex impedance of the loaded coil was 50Ω+jX (the resistance of the coil was 50Ω and the reactance was a positive value). When the coil was at 50Ω real, the tuning capacitance was increased until the reactance was minimized (became zero). The problem with this implementation of the algorithm is that both the tuning and matching capacitors are real and have real losses, and therefore, the matching capacitor needed adjustment during the tuning phase. It was easy to implement and account for these losses by adding complex impedance thresholds during the tuning phase of the analytical algorithm Basically, the coil’s complex impedance reaches 50Ω+jX the tuning capacitance was increased until the resistance of the coil was 52Ω real or greater. At this point the matching capacitance was decreased until the resistance of the coil was 48Ω real or less (at this point the tuning capacitance would be increased again). There is one significant problem with this approach, namely determining the appropriate step size during the tuning phase can be difficult. Choosing a small step size keeps the complex impedance of the coil within the designed thresholds, however significantly increases the

tuning and matching time. With a large step size, often the algorithm would not converge as change in the coils complex impedance would be too significant

6.5 CONCLUSSION

Here, a separated surface sixteen-channel transmit-only TEM array and a thirty-two-loop receive-only receiver array were designed and built for body imaging applications at 7T. It was believed between the increased transmit efficiency associated with local surface arrays and exceedingly high receiver channel count combined with the improved parallel imaging performance associated ultra-high field strengths would provide unparalleled performance specifically for cardiac imaging applications. Here we have shown the first ever, free breathing MRI images.

Furthermore, we have shown the first attempts to completely automate the tuning and matching process for the transmit array. It is believed that automating the tuning and matching process will be one of the key issues that promote 7T becoming a clinically usable field strength. Using piezoelectric actuators, automation of the tuning and matching procedure was achieved through an electromechanical process. Tuning and matching did occur in the magnet suite with each coil being tuned using a 2D root finding algorithm in approximatel y 50s.

7. Future Work and Directions

Over the past eight years, there have been significant advancements in body imaging at 7T. Initial attempts by Vaughan et al (41) used a single channel circumscribing volume TEM coil and was successful in the sense that it showed the complexities associated with body imaging at ultra-high field strengths and provided insight to new designs required. A direct result of Vaughan's initial study was the development and design of the eight-channel TEM surface array that was initially used for cardiac and prostate imaging. This quickly progressed to ah sixteen-channel surface array that is still considered a gold standard at for body imaging at 7T. Later, to improve SNR a thirty-two channel loop receiver was designed and used in conjunction with large volume array; unfortunately the volume array was not optimized and study suffered.

Those results lead to the current design, state-of-the art, surface array reported in chapter 6. Here the sixteen-channel TEM transmit-only array is coupled with a thirty-two channel loop receive-only array. Initial results have shown this array to show significant improvements in body imaging, namely with regards to increase SNR and vast improvements in parallel imaging when compared to the sixteen-channel transceiver TEM array. Additional and future studies, however, are needed to confirm this. It is believed this combined transmit-only, receive-only array will be the future direction of all body arrays at 7T until a large circumscribing transmit array is viable.

The initial result of Vaughan's study and the eight- and sixteen-channel surface array studies also realized the importance of subject specific tuning and matching. Not tuning and matching on each and every individual prior to imaging can and has shown

reductions in transmit efficiency, increased SAR and tissue heating, reduced SNR, reduced parallel imaging results, increased coupling, greater chances of damaging power amplifies and damage to the transmit array. To mitigate these dangers, to date, most surface arrays have been manually tuned and matched, however, the problem with manually tuning and matching each coil in the array is that it is time consuming and tedious and prone to user error. Of course these problems increase and propagate as the number of channels in the array increases. Automating the tuning and matching process would address and possibly alleviate these problems. To investigate the possibility of automating the tuning and matching process, an electromechanical solution was developed. Here, piezoelectric actuators were fastened to sliding cylindrical tuning and matching capacitors. Piezoelectric motors are one of the few motors that can work in strong magnetic fields; the actuators were used to manipulate and change the surface area between the center and outer plate of the cylindrical capacitors, thus changing the capacitance. This was paired with a feedback loop that monitored the reflection coefficient of the coil being tuned. The efficiency and effectiveness of this method was investigated.

This form of automating the tuning and matching process is in its infancy. The study shown above was a proof of theory. With that being said, the study did showed very favorable results. The piezoelectric actuated tuning and matching method was able to reliable tune and match the array on a load specific manner. The piezoelectric actuated tuning and matching method was able to reliable tune and match the array faster then

manual tuning and matching. The piezoelectric actuated tuning and matching method was able to reliable tune and match the array without user intervention.

Further studies into the piezoelectric automated tuning and matching process should be focused on decreasing the tune and match time through increased piezocontrollers and improved tuning and matching algorithms. Additionally the feasibility to use the sliding cylindrical capacitor coupled to a piezoelectric actuator load specific decoupling should be investigated.

8. References

1. Vaughan JT, Hetherington HP, Otu JO, Pan JW, Pohost GM. High frequency volume coils for clinical NMR imaging and spectroscopy. Magn Reson Med 1994;32(2):206-218.
2. Vaughan JT, Adriany G, Snyder CJ, Tian J, Thiel T, Bolinger L, Liu H, DelaBarre L, Ugurbil K. Efficient high-frequency body coil for high-field MRI. Magn Reson Med 2004;52(4):851-859.
3. Adriany G, Van de Moortele PF, Wiesinger F, Moeller S, Strupp JP, Andersen P, Snyder C, Zhang X, Chen W, Pruessmann KP, Boesiger P, Vaughan T, Ugurbil K. Transmit and receive transmission line arrays for 7 Tesla parallel imaging. Magn Reson Med 2005;53(2):434-445.
4. Snyder CJ, Delabarre L, Moeller S, Tian J, Akgun C, Van de Moortele PF, Bolan PJ, Ugurbil K, Vaughan JT, Metzger GJ. Comparison between eight- and sixteen-channel TEM transceive arrays for body imaging at 7 T. Magn Reson Med.
5. Lee RF, Hardy CJ, Sodickson DK, Bottomley PA. Lumped-element planar strip array (LPSA) for parallel MRI. Magn Reson Med 2004;51(1):172-183.
6. Lee RF, Westgate CR, Weiss RG, Newman DC, Bottomley PA. Planar strip array (PSA) for MRI. Magn Reson Med 2001;45(4):673-683.
7. Gupta KC, Garg R, Bahl IJ, Bhartia P. Microstrip lines and slotlines. Boston: Artech House; 1996. xvi, 535 p. p.
8. Akgun C, DelaBarre L, Yoo H, Sohn S, Snyder C, Adriany G, Van deMoortele P-F, Gopinath A, Ugurbil K, Vaughan JT. Stepped Impedance Resonators for High-Field MRI. In: Proceedings of the 20th Annual Meeting of ISMRM. Montreal2011.
9. Earls JP, Ho VB, Foo TK, Castillo E, Flamm SD. Cardiac MRI: recent progress and continued challenges. J Magn Reson Imaging 2002;16(2):111-127.
10. Pennell DJ, Sechtem UP, Higgins CB, Manning WJ, Pohost GM, Rademakers FE, van Rossum AC, Shaw LJ, Yucel EK, Society for Cardiovascular Magnetic R, Working Group on Cardiovascular Magnetic Resonance of the European Society of C. Clinical indications for cardiovascular magnetic resonance (CMR): Consensus Panel report. Eur Heart J 2004;25(21):1940-1965.
11. Lima JA, Desai MY. Cardiovascular magnetic resonance imaging: current and emerging applications. J Am Coll Cardiol 2004;44(6):1164-1171.
12. Edelman RR. Contrast-enhanced MR imaging of the heart: overview of the literature. Radiology 2004;232(3):653-668.
13. Nayak KS, Cunningham CH, Santos JM, Pauly JM. Real-time cardiac MRI at 3 tesla. Magn Reson Med 2004;51(4):655-660.
14. Weiger M, Pruessmann KP, Boesiger P. Cardiac real-time imaging using SENSE. SENSitivity Encoding scheme. Magn Reson Med 2000;43(2):177-184.
15. Wagner A, Mahrholdt H, Sechtem U, Kim RJ, Judd RM. MR imaging of myocardial perfusion and viability. Magnetic resonance imaging clinics of North America 2003;11(1):49-66.

16. Poon M, Fuster V, Fayad Z. Cardiac magnetic resonance imaging: a "one-stop-shop" evaluation of myocardial dysfunction. Current opinion in cardiology 2002;17(6):663-670.
17. Danias PG, Stuber M, Botnar RM, Kissinger KV, Yeon SB, Rofsky NM, Manning WJ. Coronary MR angiography clinical applications and potential for imaging coronary artery disease. Magnetic resonance imaging clinics of North America 2003;11(1):81-99.
18. Li D, Carr JC, Shea SM, Zheng J, Deshpande VS, Wielopolski PA, Finn JP. Coronary arteries: magnetization-prepared contrast-enhanced three-dimensional volume-targeted breath-hold MR angiography. Radiology 2001;219(1):270-277.
19. Stuber M, Botnar RM, Fischer SE, Lamerichs R, Smink J, Harvey P, Manning WJ. Preliminary report on in vivo coronary MRA at 3 Tesla in humans. Magn Reson Med 2002;48(3):425-429.
20. Liu H, Zhang J. An efficient MR phosphorous spectroscopic localization technique for studying ischemic heart. J Magn Reson Imaging 1999;10(5):892-898.
21. Zhang J, From AH, Ugurbil K, Bache RJ. Myocardial oxygenation and high-energy phosphate levels during KATP channel blockade. Am J Physiol Heart Circ Physiol 2003;285(4):H1420-1427.
22. Beer M, Sandstede J, Landschutz W, Viehrig M, Harre K, Horn M, Meininger M, Pabst T, Kenn W, Haase A, von Kienlin M, Neubauer S, Hahn D. Altered energy metabolism after myocardial infarction assessed by 31P-MR-spectroscopy in humans. Eur Radiol 2000;10(8):1323-1328.
23. Chida K, Saito H, Nagasaka T, Otani H, Kohzuki M, Zuguchi M. Rapid-sequence phosphorus-31 magnetic resonance spectroscopy of the human heart using a 1.5-T clinical system. Acta Radiol 2004;45(1):30-37.
24. Hinton DP, Wald LL, Pitts J, Schmitt F. Comparison of cardiac MRI on 1.5 and 3.0 Tesla clinical whole body systems. Invest Radiol 2003;38(7):436-442.
25. Noeske R, Seifert F, Rhein KH, Rinneberg H. Human cardiac imaging at 3 T using phased array coils. Magn Reson Med 2000;44(6):978-982.
26. Van de Moortele P-F, Snyder C, DelaBarre L, Akgun C, Wu X, Vaughan JT, Ugurbil K,. Fast mapping of relative B1+ phase in the human head at 9.4 Tesla with a 14 channel transceive coil array.In: Internation Symposium on Biomedical Magnetic Resonance Imaging and Spectroscopy at Very High Fields, . 2006; Wuerzburg, Germany. p 37.
27. Van de Moortele PF, Akgun C, Adriany G, Moeller S, Ritter J, Collins CM, Smith MB, Vaughan JT, Ugurbil K. B(1) destructive interferences and spatial phase patterns at 7 T with a head transceiver array coil. Magn Reson Med 2005;54(6):1503-1518.
28. Metzger GJ, Snyder C, Akgun C, Vaughan T, Ugurbil K, Van de Moortele PF. Local B1+ shimming for prostate imaging with transceiver arrays at 7T based on subject-dependent transmit phase measurements. Magn Reson Med 2008;59(2):396-409.

29. DelaBarre L SC, Van de Moortele P-F,, Akgun C, Ugurbil, Vaughan J,. Cardiac Imaging at 7T. In: Proceedings of the 15th Annual Meeting of ISMRM. 2007; Berlin, Germany. p 3867.
30. Snyder C, DelaBarre L, Van de Moortele P-F, Styczynski Snyder A, Akgun C, Tian J, Metzger G, Ugurbil K, Vaughan J. Stripline/TEM Transceiver Array for 7T Body Imaging. In: Proceedings of the 16th Annual Meeting of ISMRM. Berlin2007. p 164.
31. Jin JM, Chen J, Chew WC, Gan H, Magin RL, Dimbylow PJ. Computation of electromagnetic fields for high-frequency magnetic resonance imaging applications. Phys Med Biol 1996;41(12):2719-2738.
32. Huyer W NA. Global optimzation by a multilevel coordinate search. Journal Global Optimization 1999;14:24.
33. Collins CM, Smith MB. Signal-to-noise ratio and absorbed power as functions of main magnetic field strength, and definition of "90 degrees " RF pulse for the head in the birdcage coil. Magn Reson Med 2001;45(4):684-691.
34. Cunningham CH, Pauly JM, Nayak KS. Saturated double-angle method for rapid B1+ mapping. Magn Reson Med 2006;55(6):1326-1333.
35. Wu X cT-H, , Luo Z-Q,, Akgun C, Vaughan J, Ugurbil K, Van de Moortele P-F. Worst case SAR scenario as a new metric for SAR analysis in B1 phase shim. In: Proceedings of the 16th Annual Meeting of ISMRM 2008; Toronto, Canada.
36. Brunner DO, De Zanche N, Frohlich J, Paska J, Pruessmann KP. Travelling-wave nuclear magnetic resonance. Nature 2009;457(7232):994-998.
37. Chang G, Friedrich KM, Wang L, Vieira RL, Schweitzer ME, Recht MP, Wiggins GC, Regatte RR. MRI of the wrist at 7 tesla using an eight-channel array coil combined with parallel imaging: preliminary results. J Magn Reson Imaging;31(3):740-746.
38. Krug R, Carballido-Gamio J, Banerjee S, Stahl R, Carvajal L, Xu D, Vigneron D, Kelley DA, Link TM, Majumdar S. In vivo bone and cartilage MRI using fully-balanced steady-state free-precession at 7 tesla. Magn Reson Med 2007;58(6):1294-1298.
39. Snyder CJ, DelaBarre L, Metzger GJ, van de Moortele PF, Akgun C, Ugurbil K, Vaughan JT. Initial results of cardiac imaging at 7 Tesla. Magn Reson Med 2009;61(3):517-524.
40. van Elderen SG, Versluis MJ, Webb AG, Westenberg JJ, Doornbos J, Smith NB, de Roos A, Stuber M. Initial results on in vivo human coronary MR angiography at 7 T. Magn Reson Med 2009;62(6):1379-1384.
41. Vaughan JT, Snyder CJ, DelaBarre LJ, Bolan PJ, Tian J, Bolinger L, Adriany G, Andersen P, Strupp J, Ugurbil K. Whole-body imaging at 7T: preliminary results. Magn Reson Med 2009;61(1):244-248.
42. Vaughan JT, Garwood M, Collins CM, Liu W, DelaBarre L, Adriany G, Andersen P, Merkle H, Goebel R, Smith MB, Ugurbil K. 7T vs. 4T: RF power, homogeneity, and signal-to-noise comparison in head images. Magn Reson Med 2001;46(1):24-30.

43. Ohliger MA, Grant AK, Sodickson DK. Ultimate intrinsic signal-to-noise ratio for parallel MRI: electromagnetic field considerations. Magn Reson Med 2003;50(5):1018-1030.
44. Wiesinger F, Van de Moortele PF, Adriany G, De Zanche N, Ugurbil K, Pruessmann KP. Parallel imaging performance as a function of field strength--an experimental investigation using electrodynamic scaling. Magn Reson Med 2004;52(5):953-964.
45. Yacoub E, Duong TQ, Van De Moortele PF, Lindquist M, Adriany G, Kim SG, Ugurbil K, Hu X. Spin-echo fMRI in humans using high spatial resolutions and high magnetic fields. Magn Reson Med 2003;49(4):655-664.
46. Yacoub E, Harel N, Ugurbil K. High-field fMRI unveils orientation columns in humans. Proc Natl Acad Sci U S A 2008;105(30):10607-10612.
47. Yacoub E, Shmuel A, Logothetis N, Ugurbil K. Robust detection of ocular dominance columns in humans using Hahn Spin Echo BOLD functional MRI at 7 Tesla. Neuroimage 2007;37(4):1161-1177.
48. Yacoub E, Van De Moortele PF, Shmuel A, Ugurbil K. Signal and noise characteristics of Hahn SE and GE BOLD fMRI at 7 T in humans. Neuroimage 2005;24(3):738-750.
49. Duyn JH, van Gelderen P, Li TQ, de Zwart JA, Koretsky AP, Fukunaga M. High-field MRI of brain cortical substructure based on signal phase. Proc Natl Acad Sci U S A 2007;104(28):11796-11801.
50. Yao B, Li TQ, Gelderen P, Shmueli K, de Zwart JA, Duyn JH. Susceptibility contrast in high field MRI of human brain as a function of tissue iron content. Neuroimage 2009;44(4):1259-1266.
51. Adriany G, Van de Moortele PF, Ritter J, Moeller S, Auerbach EJ, Akgun C, Snyder CJ, Vaughan T, Ugurbil K. A geometrically adjustable 16-channel transmit/receive transmission line array for improved RF efficiency and parallel imaging performance at 7 Tesla. Magn Reson Med 2008;59(3):590-597.
52. Burgess RE, Yu Y, Abduljalil AM, Kangarlu A, Robitaille PM. High signal-to-noise FLASH imaging at 8 Tesla. Magn Reson Imaging 1999;17(8):1099-1103.
53. Vaughan T, DelaBarre L, Snyder C, Tian J, Akgun C, Shrivastava D, Liu W, Olson C, Adriany G, Strupp J, Andersen P, Gopinath A, van de Moortele PF, Garwood M, Ugurbil K. 9.4T human MRI: preliminary results. Magn Reson Med 2006;56(6):1274-1282.
54. Rooney WD, Johnson G, Li X, Cohen ER, Kim SG, Ugurbil K, Springer CS, Jr. Magnetic field and tissue dependencies of human brain longitudinal 1H2O relaxation in vivo. Magn Reson Med 2007;57(2):308-318.
55. Kang CK, Park CW, Han JY, Kim SH, Park CA, Kim KN, Hong SM, Kim YB, Lee KH, Cho ZH. Imaging and analysis of lenticulostriate arteries using 7.0-Tesla magnetic resonance angiography. Magn Reson Med 2009;61(1):136-144.
56. Van de Moortele PF, Auerbach EJ, Olman C, Yacoub E, Ugurbil K, Moeller S. T1 weighted brain images at 7 Tesla unbiased for Proton Density, T2* contrast and RF coil receive B1 sensitivity with simultaneous vessel visualization. Neuroimage 2009;46(2):432-446.

57. Yang QX, Wang J, Zhang X, Collins CM, Smith MB, Liu H, Zhu XH, Vaughan JT, Ugurbil K, Chen W. Analysis of wave behavior in lossy dielectric samples at high field. Magn Reson Med 2002;47(5):982-989.
58. Styczynski Snyder AL, Snyder C, Van de Moortele P-F, DelaBarre L, Haddidin IS, Truskinovky A, Vaughan JT, Ugurbil K, Garwood M, Michaeli S. Endometrial imaging at high magnetic fields: feasibility of in vivo studies at 7T. In: Proceedings of the 16th Annual Meeting of ISMRM 2007:573.
59. Styczynski-Snyder AL, Snyder CJ, DelaBarre L, Van de Moortele P-F, Vaughan JT, Ugurbil K, Garwood M, Bolan PJ. Preliminary Experience with Liver MRI and 1H MRS at 7 tesla. In: Proceedings of the 16th Annual Meeting of ISMRM. Berlin2007. p 729.
60. Snyder C DL, Van de Moortele P-F,, Styczynski Snyder A, Akgun C, Tian J, Metzger G, Ugurbil K, Vaughan JT. Stripline/TEM transceiver array for 7T body imaging. In: Proceedings of the 15th Annual Meeting of ISMRM. 2007; Berlin, Germany. p 164.
61. Orzada S, Maderwald S, Oehmigen M, Ladd M, Solbach K, Bitz A. An 8-Channel TX, 16-Channel Flexible Body Coil at 7 Tesla Using Both Branches of Centrally Fed Strip Lines as Individual Receive Elements. In: Proceedings of the 18th Annual Meeting of ISMRM. Stockholm 2010. p 641.
62. Raaijmakers A, Ipek O, Klomp D, Kroeze H, van de Bank B, Boer V, Harvey P, Possanzini C, Lagendijk J, van den Berg N. High-Field Imaging at Low SAR: Tx/Rx Prostate Coil Array Using Radiative Elements for Efficient Antenna-Patient Power Transfer. In: Proceedings of the 18th Annual Meeting of ISMRM. Stockholm 2010. p 48.
63. Umutlu L, Orzada S, Kinner S, Maderwald S, Brote I, Bitz AK, Kraff O, Ladd SC, Antoch G, Ladd ME, Quick HH, Lauenstein TC. Renal imaging at 7 Tesla: preliminary results. Eur Radiol;21(4):841-849.
64. Yarnykh VL. Actual flip-angle imaging in the pulsed steady state: a method for rapid three-dimensional mapping of the transmitted radiofrequency field. Magn Reson Med 2007;57(1):192-200.
65. Pruessmann KP, Weiger M, Scheidegger MB, Boesiger P. SENSE: sensitivity encoding for fast MRI. Magn Reson Med 1999;42(5):952-962.
66. Robson PM, Grant AK, Madhuranthakam AJ, Lattanzi R, Sodickson DK, McKenzie CA. Comprehensive quantification of signal-to-noise ratio and g-factor for image-based and k-space-based parallel imaging reconstructions. Magn Reson Med 2008;60(4):895-907.
67. Christ A, Kainz W, Hahn EG, Honegger K, Zefferer M, Neufeld E, Rascher W, Janka R, Bautz W, Chen J, Kiefer B, Schmitt P, Hollenbach HP, Shen J, Oberle M, Szczerba D, Kam A, Guag JW, Kuster N. The Virtual Family--development of surface-based anatomical models of two adults and two children for dosimetric simulations. Phys Med Biol;55(2):N23-38.
68. Lattanzi R, Sodickson DK, Grant AK, Zhu Y. Electrodynamic constraints on homogeneity and radiofrequency power deposition in multiple coil excitations. Magn Reson Med 2009;61(2):315-334.

69. van den Bergen B, Stolk CC, Berg JB, Lagendijk JJ, Van den Berg CA. Ultra fast electromagnetic field computations for RF multi-transmit techniques in high field MRI. Phys Med Biol 2009;54(5):1253-1264.
70. Metzger G, Simonson J, Bi X, Weale P, Zuehlsdorff S, Auerbach E, Ugurbil K, Van de Moortele P-F. Initial Experience with Non-Contrast Enhanced Renal Angiography at 7.0 Tesla. In: Proceedings of the 18th Annual Meeting of ISMRM. Stockholm2010. p 401.
71. Snyder C DL, Metzger G, Ugurbil K, Vaughan JT. 32-Channel Receive Only Array for Cardiac Imaging at 7T. Montreal, Canada2011. p 165.